arXiv:2107.07001v1 [math.OC] 14 Jul 2021

Fast Homotopy for Spacecraft Rendezvous Trajectory Optimization with Discrete Logic

Danylo Malyuta* and Behçet Açıkmeşe†
University of Washington, Seattle, Washington 98195

This paper presents a computationally efficient optimization algorithm for solving non-convex optimal control problems that involve discrete logic constraints. Traditional solution methods for these constraints require binary variables and mixed-integer programming, which is prohibitively slow and computationally expensive. This paper targets a fast solution that is capable of real-time implementation onboard spacecraft. To do so, a novel algorithm is developed that blends sequential convex programming and numerical continuation into a single iterative solution process. Inside the algorithm, discrete logic constraints are approximated by smooth functions, and a homotopy parameter governs the accuracy of this approximation. As the algorithm converges, the homotopy parameter is updated such that the smooth approximations enforce the exact discrete logic. The effectiveness of this approach is numerically demonstrated for a realistic rendezvous scenario inspired by the Apollo Transposition and Docking maneuver. In under 15 seconds of cumulative solver time, the algorithm is able to reliably find difficult fuel-optimal trajectories that obey the following discrete logic constraints: thruster minimum impulse-bit, range-triggered approach cone, and range-triggered plume impingement. The optimized trajectory uses significantly less fuel than reported NASA design targets.

Nomenclature

θ_{appch} = approach cone half-angle, rad

$\Delta t_{\max}$ = maximum pulse duration, s

$\Delta t_{\min}$ = minimum pulse duration, s

Δt_{ik} = pulse duration of i-th thruster at k-th control interval, s

Δt_{db} = buffer zone around $\Delta t_{\min}$ for the wall avoidance constraint, s

$\hat{f}_i$ = thrust direction vector for the i-th thruster

$\mathcal{F}_{\mathcal{B}}$ = body frame centered at the chaser COM

$\mathcal{F}_{\mathcal{L}}$ = LVLH frame centered at the target COM

F_{rcs} = constant thrust level generated by a thruster, N

*Ph.D. Candidate, Autonomous Controls Laboratory, Aeronautics & Astronautics, AIAA Student Member. Contact: danylo@uw.edu.
†Professor, Autonomous Controls Laboratory, Aeronautics & Astronautics, AIAA Associate Fellow. Contact: behcet@uw.edu.

$\hat{f}_i$ = body frame thrust direction of the i-th thruster

$\mathcal{I}_{\text{fr}}$ = indices of forward-facing thrusters

k' = $k-1$ for any general index k

N_c = number of control opportunities over the trajectory

n_o = orbital mean motion, rad s^{-1}

n_{rcs} = number of RCS thrusters

ω = chaser angular velocity, rad s^{-1}

r_{appch} = approach sphere radius, m

r_{plume} = plume impingement sphere radius, m

t_c = time interval between thruster firing, s

t_f = trajectory duration, s

$\varepsilon_{p_f}, \varepsilon_{v_f}, \varepsilon_{q_f}, \varepsilon_{\omega_f}$ = terminal boundary condition tolerances

J = chaser inertia matrix, kg m^2

m = chaser mass, kg

p = chaser position, m

p_0, v_0, q_0, ω_0 = initial boundary conditions

p_f, v_f, q_f, ω_f = terminal boundary conditions

q = chaser quaternion attitude

r_i = body frame position of the i-th thruster, m

v = chaser velocity, m s^{-1}

I. Introduction

Space programs have historically been deemed mature once they establish the ability to perform rendezvous and docking operations [1]. Some of the earliest programs of the United States and the Soviet Union (e.g., Gemini and Soyuz) had as their explicit goal to demonstrate the capability of performing rendezvous, proximity operations, and docking maneuvers. The ultimate objective to land humans on the moon drove the need for these capabilities. Beyond the lunar missions of the 1960s, rendezvous and docking continued to be a core technology required to construct and service space stations that were built in low Earth orbit [2]. The Shuttle program was comprised of dozens of missions for which rendezvous (and more generally, proximity operations) was an explicit mission objective. The core technology used to achieve rendezvous and docking has remained largely unchanged in the decades since the earliest maneuvers were successful. While this heritage technology is far from obsolete, it has been stated that it may be unable to meet the requirements of future missions [1]. A driving force that will require new methods is the need for a system that can perform *fully autonomous* rendezvous in several domains (e.g., low Earth orbit, low lunar orbit, etc.) [3]. Several

vehicles capable of autonomous docking are either already operational or in development, ranging from large vehicles such as the SpaceX Crew Dragon, Soyuz, and Orion [1, 3, 4], to smaller robotic vehicles for clearing orbital debris [5–7].

The objective of this paper is to present a framework for designing autonomous docking trajectories that accurately reflect the capabilities and constraints that have been historically prevalent for proximity operation missions. We view the problem as a trajectory generation problem, and compute what would be implemented as a guidance solution. In particular, we show how to model challenging *discrete logic* constraints within a continuous optimization framework. The resulting algorithm is numerically demonstrated to be sufficiently fast for ground-based use, and has the potential to be real-time capable if implemented in a compiled programming language. A link to the numerical implementation of the algorithm is provided in [8].

The open-loop generation of spacecraft docking trajectories using optimization-based methods is a relatively new field spawned by the shift towards autonomy [9]. Open-loop trajectory generation computes a complete start-to-finish trajectory, and leaves robust tracking to closed-loop feedback control. In [10, 11] the authors discuss both time- and fuel-optimal solutions with a focus on problem formulations that are conducive to on-board implementation. Their study offers an insightful view on the structure of optimality at the cost of a simplified problem statement and omission of state constraints. In [12], lossless convexification is used to generate fuel-optimal docking trajectories which account for nonconvex thrust and plume impingement constraints, albeit the thrust is not allowed to turn off. In [13], lossless convexification allows to generate bang-bang controls for minimum-time spacecraft rendezvous using differential drag, however without state constraints or spacecraft attitude dynamics. A similar relaxation is also presented in [14], where a sequential convex programming (SCP) algorithm is developed for near-field autonomous rendezvous in an arbitrary Keplerian orbit. Range-triggered approach cone and plume impingement constraints are imposed, however their activation is pre-determined through user specification rather than automatically by the algorithm. A similar solution method is considered in [15], where a rendezvous problem is solved with aerodynamic drag, gravity harmonics, and a nonconvex keep-out ellipsoid for collision avoidance. The latter constraint applies during the initial maneuvering phase, while for the final approach the keep-out zone is replaced by a convex approach cone.

In [16], an optimization framework is used to impose safety-based constraints in the case of anomalous behavior (including thruster failure) by introducing a suboptimal convex program to design safe trajectories which approximate a nonconvex mixed-integer problem using a new set of "safe" inputs. Along the same lines of mixed-integer programming, [17] solves a fuel-optimal problem subject to thrust plume and collision avoidance constraints. The authors introduce several heuristic techniques in order to fit the problem within the scope of mixed-integer linear programming, but still observe rather long solve times (over 40 minutes in some cases). More recently, [18] studied a multi-phase docking problem with several state constraints. The authors use binary variables to impose different constraints during each phase, and propose an iterative solution method with closed-form update rules. Beyond the use of mixed-integer methods, [19] proposes a randomized optimization method similar to the A^* method, while [20]

proposes a convex one-norm regularized model predictive control solution.

Notably, the aforementioned references do not consider the spacecraft attitude during trajectory generation and do not explicitly account for what is referred to as the minimum impulse-bit (MIB) of the reaction control thrusters that are used to realize the trajectories. The latter constraint refers to the fact that impulsive chemical thrusters cannot fire for an arbitrarily short duration, since there is some minimum pulse width that is inherent to the hardware. Hartley et al. [20] acknowledge this issue, but instead of explicitly enforcing the constraint, the authors use a one-norm penalty term to discourage violation of the constraint (i.e., a soft constraint). Our view is that both attitude and the MIB constraint are critical for close proximity operations such as the terminal phase of rendezvous and docking, where two spacecraft are maneuvering close to each other. We thus target an algorithm that can efficiently incorporate both effects.

A. Contributions

This paper's contribution is a numerical optimization algorithm to solve optimal control problems (OCPs) that involve a general class of discrete logic constraints. The algorithm is based on a novel arrangement of two core methodologies: sequential convex programming and numerical continuation. SCP is a trust region method for solving general nonconvex optimal control problems [9]. However, it is incapable of handling discrete constraints in their pure (integer) form. By using a homotopy map based on the multinomial logit function, we embed smooth approximations of discrete constraints into the SCP framework, a process also known as continuous embedding [21]. The homotopy map is then updated via a numerical continuation scheme, which transforms an initial coarse approximation into an arbitrarily precise representation of the discrete logic. Herein lies our key innovation: we run SCP and numerical continuation *in parallel*, rather than in the traditional sequenced approach where one homotopy update is followed by a full SCP solve. For this reason, we call the method *embedded* numerical continuation. The resulting algorithm is shown to converge quickly and reliably for a representative terminal rendezvous problem inspired by the Apollo Transposition and Docking maneuver. The problem involves the following major constraints: full six degree of freedom (DOF) dynamics, thruster minimum impulse-bit, range-triggered approach cone, and range-triggered plume impingement. The latter constraints are similar to those considered in [14, 15], with the advantage that discrete logic allows the approach cone and plume impingement constraints to be switched on/off *automatically* by the algorithm, without user input.

This paper represents a significant upgrade in terms of both runtime performance and convergence reliability over the same authors' previous publication on SCP-based rendezvous [26]. Figure 1 illustrates how the proposed algorithm relates to existing literature. Closest to our approach are the recently published relaxed autonomous switched hybrid system (RASHS) and composite smooth control (CSC) algorithms [22–24]. Both RASHS and CSC belong to the indirect family of methods in the sense that they solve for the optimality conditions obtained from Pontryagin's maximum principle [32–34]. Furthermore, both RASHS and CSC handle discrete logic that is representable by a sequence of Boolean and gates. Our method is distinct from RASHS and CSC in two ways. First, it is a direct method in the sense

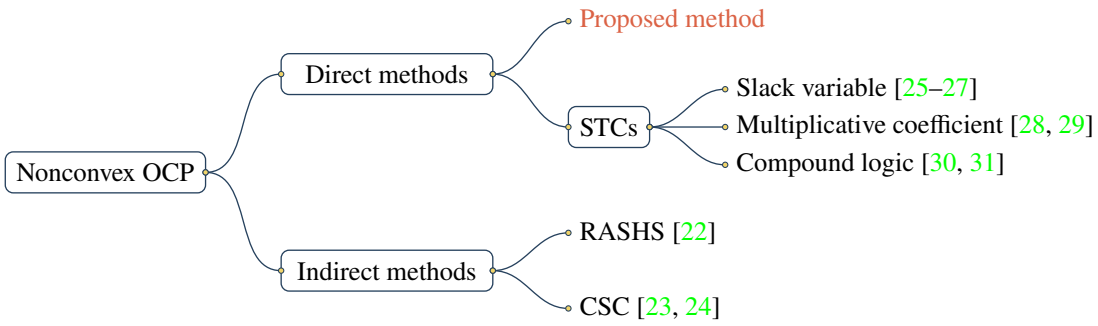


Fig. 1 Illustration of the proposed algorithm's relationship to existing literature on handling discrete logic in a continuous-variable optimization framework.

that it uses numerical optimization to solve a discretized version of the optimal control problem. This generally makes it easier to handle constraints, which are nontrivial to include in an indirect approach. Second, the proposed method models discrete logic that is representable by a sequence of Boolean `or` gates. As a result, our work combined with RASHS and CSC can extend homotopy to general Boolean logic using any combination of logic gates. A more detailed comparison of the methods is given in Section III.B.1.

Our algorithm is also closely related to the recently introduced family of state triggered constraints (STCs) for SCP algorithms [25, 28]. Unlike our method, STCs directly use linearization instead of homotopy in order to enforce an equivalent continuous-variable formulation of discrete logic constraints. Several versions of STCs have been introduced, and we cover these in more detail in Section III.A. Past work on STCs, however, discovered that they can exhibit unfavorable "locking" behavior for thruster minimum impulse-bit constraints that are relevant for spacecraft rendezvous [26]. This phenomenon prevents the algorithm from converging, and we describe it in detail in Section III.A. The algorithm presented in this article handles discrete logic constraints like STCs, and does not exhibit locking.

B. Structure

The rest of this paper is structured as follows. In Section II we formulate the rendezvous problem that is to be solved, but which is not efficiently solvable in its raw form. Section III then describes the homotopy map which can model a generic class of discrete logic in a smooth way. Using this smoothing, Section IV describes our key contribution: an algorithm that can solve nonconvex optimal control problems with discrete logic. The effectiveness of the approach is numerically demonstrated in Section V for a realistic scenario based on the historical Apollo Transposition and Docking maneuver.

The paper uses mostly standard mathematical notation. However, it is worth emphasizing the following specific notational elements. Inline vector concatenation is written as $\left[a; b; c\right] \in \mathbb{R}^3$ where $a, b, c \in \mathbb{R}$. To avoid confusion, faded text is used to denote expressions that belong to a summation, such as $\sum_{i=1}^{n} x_i + z$ where z is outside the sum. The symbol $\cup$ stands for set union, while the symbols $\wedge$ and $\vee$ represent Boolean `and` and `or` operators. Quaternion

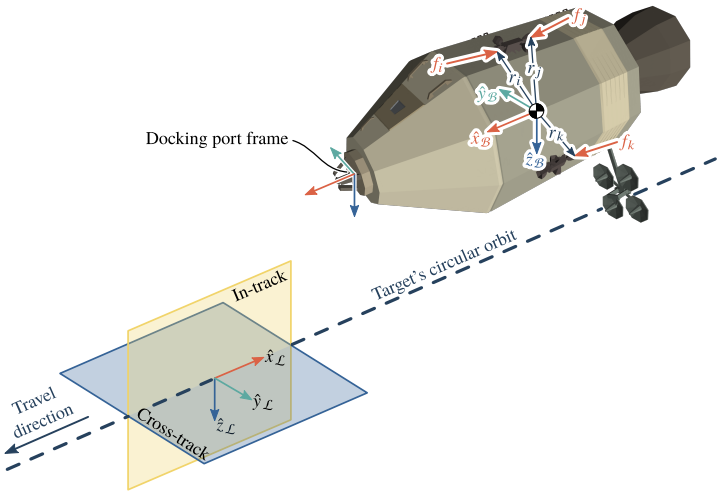


Fig. 2 The rendezvous dynamics are written in a Local-Vertical Local-Horizontal frame affixed to the target spacecraft center of mass.

multiplication is denoted by $\otimes$.

II. Rendezvous Problem Formulation

In this section we formulate a trajectory generation problem where the objective is to guide a chaser spacecraft to dock with a passive target spacecraft in a predetermined orbit. We assume that the maneuver happens in low Earth orbit (LEO) and that the target's orbit is circular. The chaser's dynamics are defined in Section II.A, the actuator model is described in Section II.B, and the rendezvous constraints are given in Sections II.C, II.D, and II.E. Section II.F gives a complete formulation of the free-final time nonconvex optimal control problem which, if solved, generates a fuel-optimal rendezvous trajectory. Most notably, because the constraints in Sections II.B, II.C, and II.D involve discrete logic, the problem is not readily solvable by traditional continuous optimization methods.

A. Chaser Spacecraft Dynamics

We begin by writing down the equations of motion for the chaser spacecraft. It is assumed that the chaser is a 6-DOF rigid body vehicle with constant mass. The latter assumption is accurate for our ultimate numerical application to the Apollo Transposition and Docking maneuver, whose fuel mass allocation is 32 kg, corresponding to about 0.1% of the total Apollo Command and Service Module (CSM) vehicle mass [35].

The general setup is illustrated in Figure 2. First, a Local-Vertical Local-Horizontal (LVLH) frame is placed at the target's center of mass (COM). Assuming that the target is in a circular orbit, and because separation distances during the final stages of rendezvous are relatively small, we can write the translation dynamics in this frame according to the

Clohessy-Wiltshire-Hill equations [36]. For the attitude dynamics, a body frame is affixed to the chaser's COM. Apart from the non-inertial forces of the relative motion dynamics in the LVLH frame, the only forces acting on the chaser are the ones generated by its system of reaction control system (RCS) thrusters. As shown in Figure 2, the force produced by each thruster is defined by its point of application r_i and its vector f_i, both of which are expressed in the $\mathcal{F}_\mathcal{B}$ frame. Altogether, the 6-DOF equations of motion of the chaser in the LVLH frame are written as follows:

$$\dot{p}(t) = v(t), \tag{1a}$$

$$\dot{v}(t) = \frac{1}{m}\sum_{i=1}^{n_{\text{rcs}}} q(t) \otimes f_i \otimes q(t)^* + a_{\text{LVLH}}\big(p(t), v(t)\big), \tag{1b}$$

$$\dot{q}(t) = \frac{1}{2} q(t) \otimes \omega(t), \tag{1c}$$

$$\dot{\omega}(t) = J^{-1}\Big[\sum_{i=1}^{n_{\text{rcs}}} r_i \times f_i(t) - \omega(t) \times \big(J\omega(t)\big)\Big], \tag{1d}$$

where the acceleration due to relative motion is given by:

$$a_{\text{LVLH}}(p, v) = \big(-2n_o \hat{z}_\mathcal{L}^\intercal v\big)\hat{x}_\mathcal{L} + \big(-n_o^2 \hat{y}_\mathcal{L}^\intercal r\big)\hat{y}_\mathcal{L} + \big(3n_o^2 \hat{z}_\mathcal{L}^\intercal r + 2n_o \hat{x}_\mathcal{L}^\intercal v\big)\hat{z}_\mathcal{L}, \tag{2}$$

where $n_o \in \mathbb{R}$ is the orbital mean motion. The translation dynamics are encoded by $p \in \mathbb{R}^3$ and $v \in \mathbb{R}^3$, which are LVLH frame vectors denoting the position and velocity of $\mathcal{F}_\mathcal{B}$ with respect to $\mathcal{F}_\mathcal{L}$. The attitude dynamics are encoded by a quaternion $q \in \mathbb{Q}$ and an angular velocity $\omega \in \mathbb{R}^3$. We use the Hamilton quaternion convention and represent q as a four-element vector [37]. The quaternion thus represents a frame transformation from $\mathcal{F}_\mathcal{B}$ to $\mathcal{F}_\mathcal{L}$, or (equivalently) the rotation of a vector in the $\mathcal{F}_\mathcal{L}$ frame. The ω vector corresponds to the angular velocity of $\mathcal{F}_\mathcal{B}$ with respect to $\mathcal{F}_\mathcal{L}$, expressed as a vector in the $\mathcal{F}_\mathcal{B}$ frame. Altogether, the vehicle state is encoded by $x = \big[p; v; q; \omega\big] \in \mathbb{R}^{13}$.

B. Impulsive Thrust Model

As mentioned in the previous section, the chaser is controlled by a system of n_{rcs} RCS thrusters. In accordance with our ultimate application to the Apollo CSM spacecraft, we assume that each thruster is able to deliver a constant thrust for a variable duration of time [38–40]. This is known as pulse-width modulation (PWM).

Let us temporarily focus the discussion on the force produced by the i-th thruster. Let F_{rcs} denote the constant thrust level generated when the thruster is active (i.e., "firing"), and let Δt_i be the firing or pulse duration. If the thruster fires for a very short duration relative to the bandwidth of the chaser's dynamics, then we can approximate the state as being constant over the firing interval. We can furthermore shrink the firing interval to zero, as long as we increase the thrust level to maintain a constant net impulse that is imparted on the chaser. This is illustrated in Figure 3, where an original 500 ms rectangular pulse is reduced down to 100 ms. In the limit as Δt_i is reduced to zero, the thrust signal becomes a

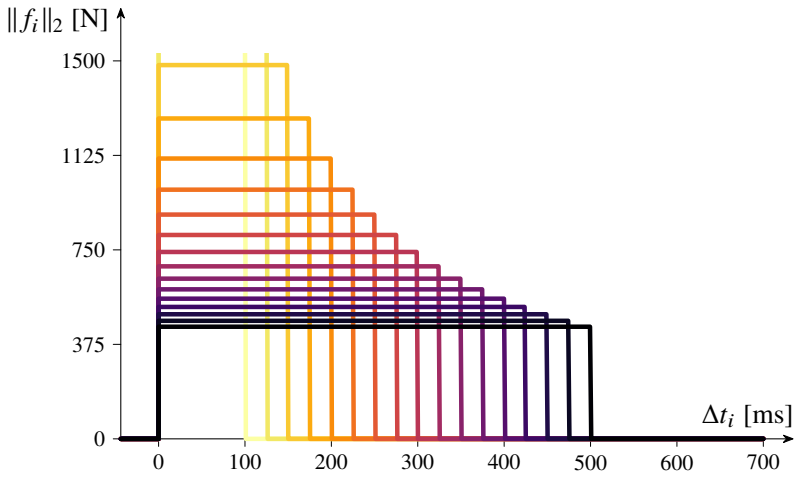


Fig. 3 Rectangular thrust pulse duration can be decreased while maintaining a constant net impulse (i.e., the area under the curve) by increasing the corresponding thrust level.

scaled Dirac delta function:

$$f_i(t) = \Delta t_i F_{\text{rcs}} \delta(t). \tag{3}$$

This model is an accurate enough approximation for generating long duration trajectories with relatively few intermittent control interventions. By neglecting state variation over the firing duration, the model furthermore has a significant computational advantage when it comes to linearizing, discretizing, and simulating the dynamics for the solution process in Section IV. We emphasize, however, that (3) is a model which we use for computation alone. In the physical world, we still expect the thrusters to fire for a finite duration and at their design (finite) thrust level.

The discussion so far has centered around a single pulse that occurs at $t = 0$ s. We now generalize this model to the trajectory generation context. Begin by fixing a control interval $t_c > 0$ that corresponds to the "silent" time interval between thruster firings. Furthermore, let N_c be the total number of control opportunities during the trajectory. This means that the trajectory lasts for $N_c t_c$ seconds. Note that no firing occurs at the final time instant, since that would lead to undesirable control at the moment of docking. Thus, a thruster can be activated only at the time instances $(k-1)t_c$ where $k = 1, 2, \ldots, N_c$. To keep the notation short, we define $k' \equiv k - 1$ for any general index k. Thus, the thrust signal for the i-th thruster can be formally written as:

$$f_i(t) = \sum_{k=1}^{N_c} \Delta t_{ik} F_{\text{rcs}} \delta\big(t - k' t_c\big) \hat{f}_i, \tag{4}$$

where Δt_{ik} is the pulse duration for the i-th thruster at the k-th control opportunity, and $\hat{f}_i$ is the thrust direction unit vector in the $\mathcal{F}_{\mathcal{B}}$ frame. Due to delays in on-board electronics and residual propellant flow downstream of the injector valves [40, pp. 2.5-16 to 2.5-18], the pulse duration is lower bounded such that $\Delta t_{ik} \geq \Delta t_{\min}$. This is known as a minimum impulse-bit (MIB) constraint. Other propulsion and RCS parameters, such as engine service life and damage

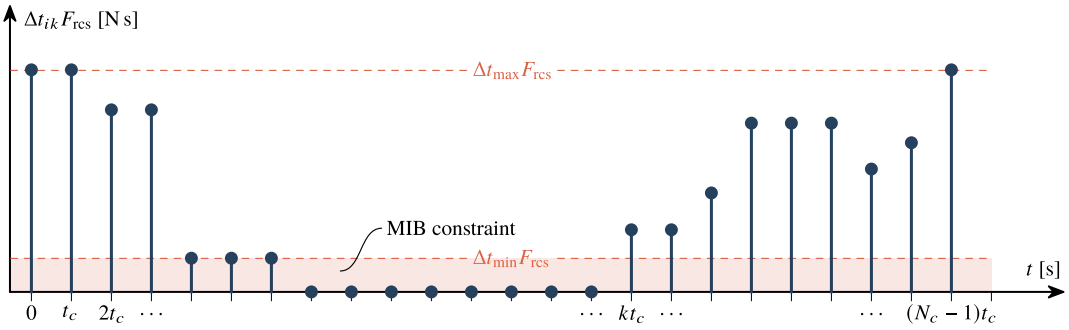


Fig. 4 Example of a control history that is compatible with the impulsive thrust model (4) and the pulse duration constraint (5).

to engine materials, impose an upper bound $\Delta t_{ik} \leq \Delta t_{\max}$. As a result, the pulse duration must satisfy the following nonconvex constraint:

$$\Delta t_{ik} \in \{0\} \cup [\Delta t_{\min}, \Delta t_{\max}]. \tag{5}$$

Figure 4 illustrates a typical control history that we can expect from the model (4) subject to the constraint (5). The salient feature of this control history is that the thruster is either silent, or firing with a minimum impulse. In particular, no impulse occurs in the MIB keep-out zone between 0 and $\Delta t_{\min} F_{\text{rcs}}$ N s. This region represents impulses which the RCS system cannot reproduce.

C. Plume Impingement Constraint

A plume impingement constraint prevents the RCS thrusters from firing and potentially damaging the target spacecraft. Naturally, this constraint is only required once the chaser is close enough to the target. Let $\mathcal{I}_{\text{fr}}$ denote the indices of forward-facing thrusters that are physically pointed along the $+\hat{x}_{\mathcal{B}}$ axis in Figure 2. Due to the physics of rendezvous and the approach cone constraint of the next section, it is reasonable to assume that large-angle maneuvering is finished by the time the spacecraft is close to the target. Thus, when the plume impingement constraint is relevant, the chaser is approximately facing the target. This yields a simple plume impingement heuristic: shut off the $\mathcal{I}_{\text{fr}}$ thrusters when the chaser is inside a so-called plume impingement sphere of radius r_{plume} centered at the target. This can be formally stated as the following implication:

$$\|p(k't_c)\|_2 \leq r_{\text{plume}} \implies \Delta t_{ik} = 0 \text{ for all } i \in \mathcal{I}_{\text{fr}}. \tag{6}$$

D. Approach Cone Constraint

The approach cone constraint bounds how much the chaser spacecraft can maneuver once it gets close enough to the target. It has the direct effect of bounding transverse motion along the $\hat{y}_{\mathcal{L}}$ and $\hat{z}_{\mathcal{L}}$ LVLH axes in Figure 2. In practice, it

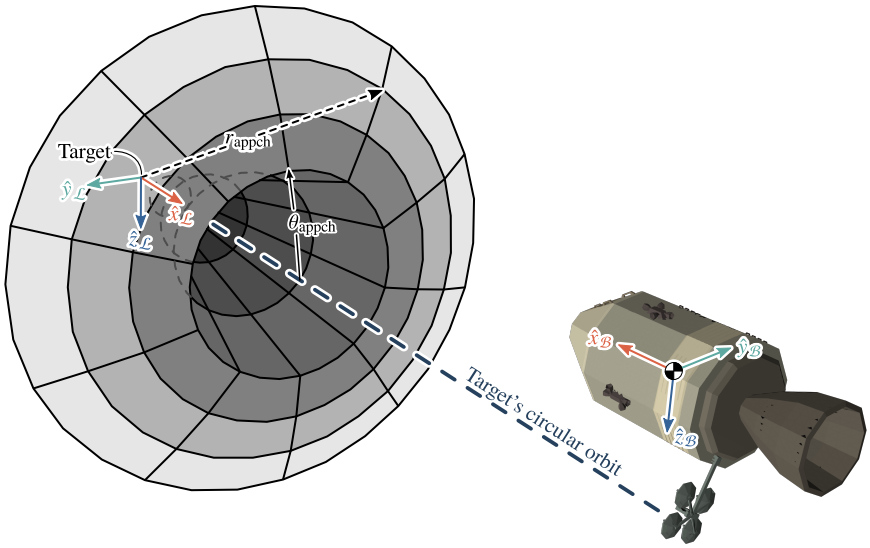


Fig. 5 The chaser's position is constrained to lie inside of an approach cone when the chaser enters an approach sphere of radius r_{appch} centered at the target (only part of the sphere is shown).

also bounds all other maneuvering, including attitude rates, except for translation motion along $-\hat{x}_{\mathcal{L}}$.

Figure 5 illustrates our implementation of an approach cone. Because we do not want to restrict the chaser's motion far away from the target, the constraint only gets applied once the chaser enters a so-called approach sphere of radius r_{appch}. When this condition is satisfied, the chaser's position is constrained to lie in a cone that emanates from the target along $+\hat{x}_{\mathcal{L}}$ and has an opening half-angle θ_{appch}. Formally, the approach cone constraint can be written as the following implication:

$$\|p(t)\|_2 \leq r_{\text{appch}} \implies \hat{x}_{\mathcal{L}}^{\mathsf{T}} p(t) \geq \|p(t)\|_2 \cos(\theta_{\text{appch}}). \tag{7}$$

E. Boundary Conditions

We consider the case of terminal rendezvous between two fixed boundary conditions: some initial chaser state and a terminal "docked" state. In particular, let $x_0 = \left[p_0; v_0; q_0; \omega_0\right] \in \mathbb{R}^{13}$ and $x_f = \left[p_f; v_f; q_f; \omega_f\right] \in \mathbb{R}^{13}$ correspond to the initial and terminal desired states. The terminal position and attitude are computed according to the relative geometry of the target and chaser docking ports and the chaser COM. For simplicity, assume that the target docking port is centered at the origin of $\mathcal{F}_{\mathcal{L}}$ and points along $+\hat{x}_{\mathcal{L}}$. Generalizing this assumption to a non-collocated docking port is possible, but does not represent anything particularly novel or challenging for our algorithm. When docked, let $q_\ell \in \mathbb{Q}$ denote the chaser docking port's attitude with respect to the target docking port. As illustrated in Figure 2, q_ℓ is a simple yaw around $+\hat{z}_{\mathcal{L}}$ by 180°. Furthermore, let $q_{\text{dp}} \in \mathbb{Q}$ and $p_{\text{dp}} \in \mathbb{R}^3$ be the rotation and position of the chaser docking port relative to $\mathcal{F}_{\mathcal{B}}$. The terminal position and attitude are then given by:

$$q_f = q_\ell \otimes q_{\text{dp}}^*, \tag{8a}$$

$$p_f = -q_f \otimes p_{\text{dp}} \otimes q_f^*. \tag{8b}$$

For a rendezvous trajectory that lasts t_f seconds, the boundary conditions we impose are:

$$x(0) = x_0, \quad x(t_f) + \Delta x_f = x_f, \tag{9}$$

where $\Delta x_f = \left[\Delta p_f; \Delta v_f; \Delta q_f; \Delta \omega_f\right] \in \mathbb{R}^{13}$ relaxes of the terminal boundary condition. This is necessary because the MIB constraint from Figure 4 makes it impossible to fine-tune the trajectory to arbitrary precision. In general, some terminal error has to occur. As long as this error is small, it will be safely absorbed by the mechanical design of the docking port. The required tolerances can be found in the spacecraft's manual. For example, for the Apollo CSM the complete list is given in [38, Section 3.8.2.3]. Because it is good practice to leave a margin of error for feedback controllers, we will constrain Δx_f to a much smaller value than what the docking mechanism can tolerate. The following constraints restrict the size of Δx_f to user-specified tolerances:

$$\|\Delta p_f\|_\infty \leq \varepsilon_{p_f}, \quad \hat{x}_{\mathcal{L}}^{\mathsf{T}} \Delta p_f = 0, \tag{10a}$$

$$\|\Delta v_f\|_\infty \leq \varepsilon_{v_f}, \tag{10b}$$

$$q(t_f)^{\mathsf{T}} q_f \geq \cos(\varepsilon_{q_f}/2), \tag{10c}$$

$$\|\Delta \omega_f\|_\infty \leq \varepsilon_{\omega_f}. \tag{10d}$$

The terminal position along $\hat{x}_{\mathcal{L}}$ is made exact since contact along $\hat{x}_{\mathcal{L}}$ is required for docking. Furthermore, it is always possible to satisfy by adjusting t_f. The terminal attitude is constrained by (10c) in terms of an error quaternion, and says that the angular deviation from q_f about any axis must be no larger than angle ε_{q_f}.

F. Basic Rendezvous Problem

Our goal is to compute a fuel-optimal rendezvous trajectory, which means that it is desirable to keep the pulse durations Δt_{ik} as short and as sparse as possible. An appropriate optimization cost function is simply the sum of pulse durations for all thrusters and control opportunities:

$$J_{\text{fuel}} = \Delta t_{\text{max}}^{-1} \sum_{i=1}^{n_{\text{rcs}}} \sum_{k=1}^{N_c} \Delta t_{ik}, \tag{11}$$

where the normalization by Δt_{max} is useful when (11) is mixed with other costs for the solution process in Section IV. Note that (11) is effectively a one-norm penalty on the pulse durations. This encourages the optimal pulse history to be sparse, which goes part of the way towards discouraging MIB constraint violation [20, 41].

We can now summarize the above sections by writing the full rendezvous optimization problem that has to be solved. We call this the basic rendezvous problem (BRP). Starting now and throughout the rest of the article, the time argument will be omitted whenever it does not introduce ambiguity.

$$\min_{x,\Delta t,t_f} \; J_{\text{fuel}} \tag{12a}$$

$$\text{s.t. } \dot{p} = v, \tag{12b}$$

$$\dot{v} = \frac{1}{m}\sum_{i=1}^{n_{\text{rcs}}} q \otimes f_i \otimes q^* + a_{\text{LVLH}}(p, v), \tag{12c}$$

$$\dot{q} = \frac{1}{2} q \otimes \omega, \tag{12d}$$

$$\dot{\omega} = J^{-1}\Big[\sum_{i=1}^{n_{\text{rcs}}} r_i \times f_i - \omega \times (J\omega)\Big], \tag{12e}$$

$$\Delta t_{ik} \in \{0\} \cup [\Delta t_{\min}, \Delta t_{\max}], \tag{12f}$$

$$\|p(k' t_c)\|_2 \leq r_{\text{plume}} \implies \Delta t_{ik} = 0 \text{ for all } i \in \mathcal{I}_{\text{fr}}, \tag{12g}$$

$$\|p\|_2 \leq r_{\text{appch}} \implies \hat{x}_{\mathcal{L}}^{\mathsf{T}} p \geq \|p\|_2 \cos(\theta_{\text{appch}}), \tag{12h}$$

$$x(0) = x_0, \quad x(t_f) + \Delta x_f = x_f, \tag{12i}$$

$$\|\Delta p_f\|_\infty \leq \varepsilon_{p_f}, \; \hat{x}_{\mathcal{L}}^{\mathsf{T}} \Delta p_f = 0, \; \|\Delta v_f\|_\infty \leq \varepsilon_{v_f}, \tag{12j}$$

$$q(t_f)^{\mathsf{T}} q_f \geq \cos(\varepsilon_{q_f}/2), \; \|\Delta \omega_f\|_\infty \leq \varepsilon_{\omega_f}. \tag{12k}$$

The BRP is a continuous-time, free-final time, nonconvex optimal control problem. It is not efficiently solvable on a computer for three main reasons [9]:

1) Continuous-time problems have an infinite number of DOFs in the optimized control signal. However, numerical optimization algorithms are restricted to a finite number of DOFs;
2) The problem has nonlinear dynamics, which results in a nonconvex optimal control problem. However, numerical algorithms for nonconvex problems require expert initial guesses and generally do not converge quickly and reliably enough for safety-critical applications [41, 42];
3) The constraints (12f)-(12h) contain discrete `if-else` logic. This is traditionally handled by mixed-integer programming (MIP), which has exponential computational complexity and does not scale well to large problems [43].

We will begin by resolving the third issue through a homotopy approach in the next section. The first two issues will then be tackled in Section IV.

III. Homotopy for Smooth Approximation of Discrete Logic

We now consider the problem of computationally efficient modeling the discrete logic constraints (12f)-(12h). This model along with the associated numerical continuation solution method in Section IV are the main contributions of this paper. We begin in Section III.A with a motivation for why a new approach to handling discrete logic is necessary. Our homotopy approach is then described in general terms in Section III.B. Finally, Sections III.C, III.D, and III.E specialize the approach to the discrete logic constraints (12f)-(12h).

A. Motivation

The traditional way of handling discrete logic in an optimization problem is through the use of binary variables [44, 45]. As a concrete example, consider the plume impingement constraint (12g). Let $\zeta_{\text{plume}}(t) : [0, t_f] \to \{0, 1\}$ denote a binary variable trajectory that is also to be optimized. Let M_{plume} be a large positive value that bounds all possible values of $\|p(t)\|_2$ that can occur during a rendezvous trajectory. For example, $M_{\text{plume}} = 10\|p_0\|_2$ is a reasonable choice. The plume impingement constraint (12g) can then be equivalently written as:

$$\zeta_{\text{plume}}(k't_c) r_{\text{plume}} \leq \|p(k't_c)\|_2 \leq r_{\text{plume}} + \zeta_{\text{plume}}(k't_c) M_{\text{plume}}, \tag{13a}$$

$$0 \leq \Delta t_{ik} \leq \zeta_{\text{plume}}(k't_c) \Delta t_{\max} \text{ for all } i \in \mathcal{I}_{\text{fr}}. \tag{13b}$$

Looking at (13), ζ_{plume} can be interpreted as follows: the chaser is outside the plume impingement sphere if and only if $\zeta_{\text{plume}} = 1$. When the chaser is inside this sphere, the only feasible choice is $\zeta_{\text{plume}} = 0$, and (13b) shuts off the forward-facing thrusters.

A similar formulation can be used to model the MIB and approach cone constraints (12f) and (12h), resulting in a MIP formulation. Unfortunately, this approach has an issue when it comes to actually solving Problem 12: mixed-integer optimization algorithms are generally too slow for real-time applications, are computationally expensive, and do not scale well to large problem sizes [43, 46]. When compounded by the fact that this formulation introduces new nonconvex constraints (e.g., the position norm lower bound in (13a)), it becomes clear that the MIP approach is not a workable real-time solution method for Problem 12.

Several methods have been proposed in recent years to replace MIP with a real-time capable approach. On the one hand, recent theoretical results have demonstrated that a lossless relaxation can solve certain classes of problems with discrete logic constraints on the control variable [47, 48]. This approach is practical because it requires solving only a single convex problem. Some versions of the method can handle restricted forms of nonlinear dynamics and convex constraints [9, 49, 50]. However, the method does not apply to the full generality of Problem 12, which involves more complicated nonlinear dynamics as well as discrete logic constraints on the state.

A separate family of solution methods has been proposed to handle discrete logic constraints using sequential

convex programming (SCP) [9]. The methods define so-called state triggered constraints (STCs) that can embed general discrete logic into a continuous optimization framework [27, 29, 51]. Two equivalent forms of STCs have been proposed, based on a slack variable [25] and based on a multiplicative coefficient that is motivated by the linear complementarity problem [28]. STCs have also been extended to handle quite general logical combinations of `and` and `or` gates [30, 31]. In fact, the authors of this paper have applied STCs to solve a version of Problem 12, with the results available in [26]. In the latter work it was observed that STCs run into an issue called *locking* for the MIB constraint (12f) [26, Definition 1]. As described in Section IV, SCP works by iteratively refining an approximate solution of Problem 12. In brief terms, locking means that once the algorithm chooses $\Delta t_{ik} = 0$ at a particular iteration, it is unable to change the value to $\Delta t_{ik} \in [\Delta t_{\min}, \Delta t_{\max}]$ at later iterations. The effect is that the algorithm is susceptible to getting into a "corner" where it is unable to use thrusters if they become needed at later refinements of the rendezvous trajectory. The consequence is failure to generate a feasible trajectory. There is currently no known remedy for constraints that exhibit locking in the STC formulations of [25, 28].

For reasons that are well documented in past literature, we view SCP as one of the most effective frameworks for the real-time solution of nonconvex trajectory generation problems [9, 51, 52]. Thus, our primary motivation is to devise a new general method that is free from locking and that can embed discrete logic into an SCP-based continuous optimization framework.

B. The Homotopy Algorithm

We now develop a homotopy-based method to systematically handle `if-else` discrete logic constraints of the following form:

$$\text{"If"} \quad L(z) \triangleq \bigwedge_{i=1}^{n_g} \big(g_i(z) \le 0\big) \implies f_L(z) \le 0, \tag{14a}$$

$$\text{"Else"} \quad R(z) \triangleq \bigvee_{i=1}^{n_g} \big(g_i(z) > 0\big) \implies f_R(z) \le 0, \tag{14b}$$

where $z \in \mathbb{R}^{n_z}$ is a generic placeholder for one or several optimization variables. The functions $g_i : \mathbb{R}^{n_z} \to \mathbb{R}$ are called predicates, and the functions $f_L : \mathbb{R}^{n_z} \to \mathbb{R}^{n_f}$ and $f_R : \mathbb{R}^{n_z} \to \mathbb{R}^{n_f}$ are implication constraints to be enforced when the corresponding expression's left-hand side is `true`. For (14a) this is a combination of `and` gates, whereas for (14b) it is a combination of `or` gates with the predicate inequalities reversed. We may thus see (14) in the following light: enforce $f_L \le 0$ when *all* the predicates are nonpositive, or enforce $f_R \le 0$ when *any* predicate is positive.

One can show using De Morgan's theorem that $R(z) = \neg L(z)$. As a result, the implications in (14) indeed form an `if-else` pair in the sense that exactly one of f_L and f_R is enforced at any given instant. The situation is illustrated in Figure 6. In the predicate space, the functions g_i form sublevel sets of nonpositive values. In the implication space,

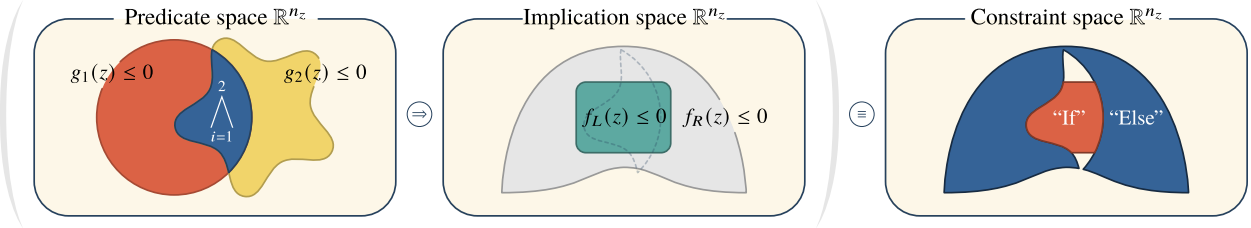


Fig. 6 Pictorial representation of the `if-else` discrete logic constraint (14).

the constraint functions f_L and f_R also form sublevel sets of nonpositive values. Note that these sets can generally be disjoint. The overall `if` constraint is obtained by intersecting the sublevel set of f_L with the sublevel set of the `and` combination. Conversely, the overall `else` constraint is obtained by intersecting the sublevel set of f_R with the complement of the sublevel set for the `and` combination.

By using the value 1 to denote `true` and 0 to denote `false`, we have the complementarity relationship $R(z) = 1 - L(z)$. Using this property, (14) can be stated in the following equivalent ways:

$$L(z) f_L(z) + \big[1 - L(z)\big] f_R(z) \le 0, \tag{15a}$$

$$\big[1 - R(z)\big] f_L(z) + R(z) f_R(z) \le 0. \tag{15b}$$

Because (15) involves discrete elements (i.e., the `and` and `or` gates), it cannot be readily included in a continuous optimization problem. As mentioned in the previous section, STCs are one possible way to circumvent the issue, however they exhibit locking in the particular case of the MIB constraint (12f). An alternative approach is to replace either L or R by a smooth approximation, and to apply a numerical continuation scheme to iteratively improve the approximation until some arbitrary precision [42]. We take this latter approach, and begin with a brief description of two existing methods.

1. Existing Homotopy Methods

Homotopy is the core idea behind the recent relaxed autonomous switched hybrid system (RASHS) and composite smooth control (CSC) algorithms [22–24]. Both algorithms model the constraint (15a) by approximating the `and` combination with a sigmoid function. To this end, let $\sigma_\kappa(w) : \mathbb{R} \to \mathbb{R}$ represent a sigmoid function which approaches one for negative arguments and zero for positive arguments. The transition point occurs at $w = 0$ and the homotopy parameter $\kappa > 0$ (also known as a sharpness parameter) regulates how quickly the transition happens. As κ increases, σ_κ approaches a "step down" function. This allows RASHS and CSC to model L as follows:

$$L(z) \approx \tilde{L}_\kappa(z) \triangleq \prod_{i=1}^{n_g} \sigma_\kappa\big(g_i(z)\big). \tag{16}$$

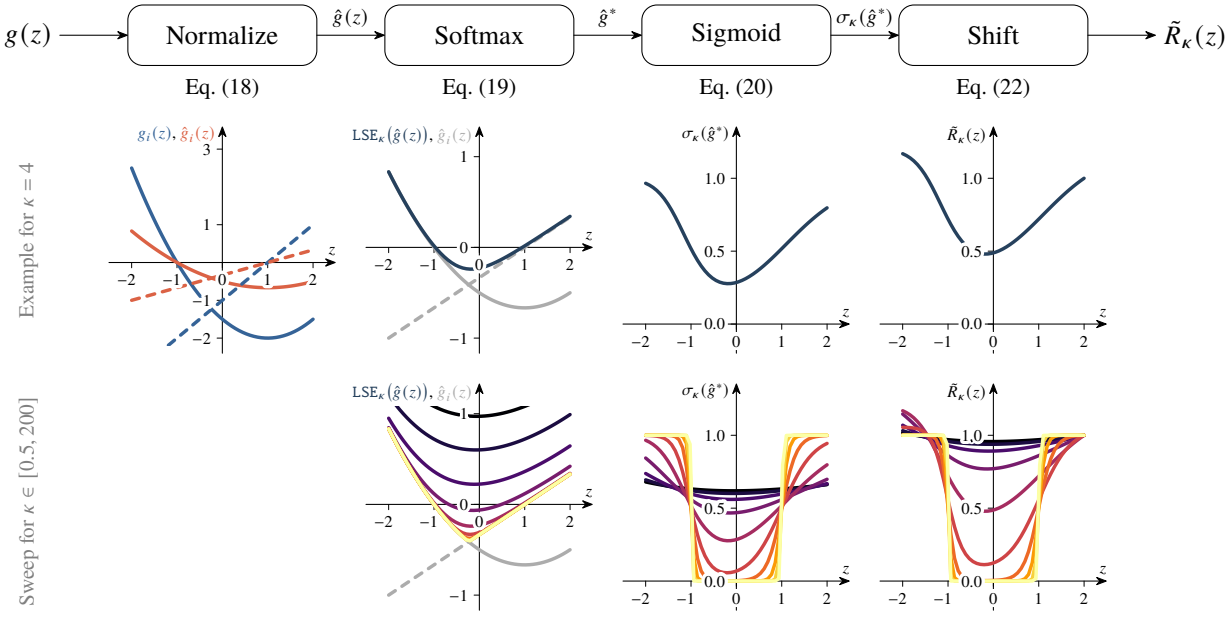


Fig. 7 Illustration for a simple set of two predicates (blue curves in the second row, first column) of the four stages comprising our smooth approximation of the `or` combination in (14b).

By replacing L with $\tilde{L}_\kappa$ in (15a), the RASHS and CSC methods can model discrete logic in a smooth way that is conducive for continuous optimization. By using numerical continuation to progressively increase κ, the methods can enforce the discrete logic constraint (15a) with arbitrary accuracy.

2. *Proposed Homotopy Method*

Our method for imposing (14) is centered around a smooth approximation of the alternative constraint (15b) using a multinomial logit function [53]. We thus view our approach as a "dual" formulation to RASHS and CSC: instead of modeling the `and` combination of (14a), we model its complement (14b). A noteworthy benefit of this approach is the ability to model `or` combinations, whereas RASHS and CSC both appear to be compatible only with `and` logic. Our method is therefore an extension of the ideas in RASHS and CSC. Although we do not develop the full theory here, our method together with (16) can model arbitrary combinations of `and` and `or` logic. This extends smooth modeling of discrete logic to its full generality.

We break down the smooth approximation of R into four computational "stages". The reader may follow along with the help of the illustration in Figure 7. Begin with the raw data, which are the individual predicate values $g_i(z)$. For convenience, let $g(z) : \mathbb{R}^{n_z} \to \mathbb{R}^{n_g}$ be the concatenated vector of predicates. The first stage is to normalize $g(z)$ by the expected maximum value of the predicates:

$$g_{\max} \triangleq \max_z \|g(z)\|_\infty, \tag{17}$$

where z is understood to be taken from the set of all reasonable values for Problem 12. We can then define a normalized predicate vector:

$$\hat{g}(z) \triangleq g_{\max}^{-1} g(z). \tag{18}$$

Normalization ensures that $\hat{g}(z)$ takes values in a $[-1, 1]^{n_g}$ hypercube. This helps to standardize the parameter choices for the numerical continuation solution method, which we will describe in Section IV. The second stage is to pick out the maximum predicate value. Because we want a smooth approximation, we find an approximate maximum using the log-sum-exp function, also known as a softmax. For a given homotopy parameter $\kappa > 0$, the softmax function $\mathtt{LSE}_\kappa : \mathbb{R}^{n_g} \to \mathbb{R}$ is defined by:

$$\mathtt{LSE}_\kappa\big(\hat{g}(z)\big) \triangleq \kappa^{-1} \log\Big(\sum_{i=1}^{n_g} e^{\kappa \hat{g}_i(z)}\Big). \tag{19}$$

Let us denote the resulting value by $\hat{g}^* \equiv \mathtt{LSE}_\kappa\big(\hat{g}(z)\big)$. As κ grows, this value approaches the true $\max_i \hat{g}_i(z)$. In the third stage, the value is passed to a sigmoid function which maps it to the $[0, 1]$ interval. This function approaches zero for negative arguments and one for positive arguments. We define it as follows:

$$\sigma_\kappa(\hat{g}^*) \triangleq 1 - \left[1 + e^{\kappa \hat{g}^*}\right]^{-1}. \tag{20}$$

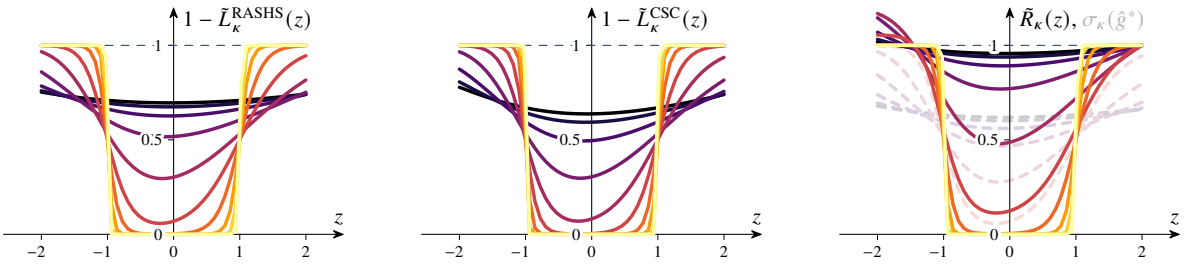
Note that by subtituting (19) into (20), we obtain the familiar multinomial logit function [53]:

$$\sigma_\kappa(\hat{g}^*) = 1 - \left[1 + \sum_{i=1}^{n_g} e^{\kappa \hat{g}_i}\right]^{-1}. \tag{21}$$

For this reason, we call our approach *multinomial logit smoothing*. When κ is large and the time comes to computing the derivatives of (21) for the solution process in Section IV, we have noted that there are important numerical stability advantages to breaking the logistic function into separate steps (19) into (20). This is why we keep the second and third stages separate.

The fourth and last stage of approximating R is to vertically shift the sigmoid function so that it matches its exact value at some specified predicate value $g_c \in \mathbb{R}^{n_g}$, where we require at least one element to be positive (such that $R(z) > 0$). We typically choose $g_c = g(z^*)$ where $z^* = \operatorname{argmax}_z \|g(z)\|_\infty$ from (17). Shifting carries the benefit of not over-restricting the solution variables early in the solution process, when κ is small and $\sigma_\kappa \approx n_g/(n_g + 1)$. The latter effect is visible in the bottom row, third column of Figure 7. Ultimately, the smooth approximation of R is defined as follows, and is the direct counterpart of the RASHS and CSC model (16):

$$R(z) \approx \tilde{R}_\kappa(z) \triangleq \sigma_\kappa(\hat{g}^*) + \big(1 - \sigma_\kappa(g_c)\big). \tag{22}$$



(a) The RASHS method [22]. **(b) The CSC method [23, 24].** **(c) Our proposed method (22).**

Fig. 8 Comparison of smoothed discrete `or` logic (14b) obtained using three smoothing methods. Faint dashed lines in (c) show the multinomial logit function (21) without shifting, which is very similar to RASHS in (a).

The discrete logic constraint (14) can then be written as the following smooth approximation, which is obtained by substituting R in (15b) with $\tilde{R}_\kappa$ from (22):

$$\left[1 - \tilde{R}_\kappa(z)\right] f_L(z) + \tilde{R}_\kappa(z) f_R(z) \leq 0. \tag{23}$$

In the following sections, we will show how to use (23) to model the discrete logic constraints (12f)-(12h). For the sake of comparison, the RASHS and CSC smooth approximations (16) are given by [22, 23]:

$$\tilde{L}_\kappa^{\text{RASHS}}(z) = \prod_{i=1}^{n_g} \left(1 + e^{\kappa \hat{g}_i(z)}\right)^{-1}, \tag{24a}$$

$$\tilde{L}_\kappa^{\text{CSC}}(z) = \prod_{i=1}^{n_g} \frac{1}{2}\left(1 - \tanh\left(\kappa \hat{g}_i(z)\right)\right). \tag{24b}$$

Figure 8 compares the smooth logic (24) with our approach (22). Without the shifting operation in (22), all three methods are remarkably similar. Multinomial logit smoothing without shifting is most similar to RASHS: the two methods are identical for $n_g = 1$, and slightly different for $n_g > 1$. Thus, shifting is the critical difference in our method. As we shall see below, it is most critical for constraints like the MIB (12f), where it is important that $\tilde{R}_\kappa(z) \approx 1$ for small κ (this effectively removes the MIB constraint from the early solution algorithm iterations in Section IV).

C. Modeling the Approach Cone

We begin by modeling the approach cone constraint (12h) in the framework of (14) and its smooth approximation (23). Comparing (12h) with (14a), we have $n_g = 1$, $z = p$, and the predicate:

$$g_1(p) = p^\intercal p - r_{\text{appch}}^2, \tag{25}$$

where we use the two-norm squared to conveniently make the predicate everywhere smooth. This predicate is then used in (22) to form $\tilde{R}_\kappa^{\text{appch}}$, the smooth `or` approximation for the approach cone predicate. The `if` implication can be written

as:

$$f_L(p) = \cos(\theta_{\text{appch}}) - \hat{x}_{\mathcal{L}}^{\mathsf{T}} p \|p\|_2^{-1}. \tag{26}$$

When the chaser is outside of the approach sphere, we wish to allow the chaser's trajectory to assume any approach angle. By the Cauchy-Schwarz inequality, this can be expressed as the inequality $\hat{x}_{\mathcal{L}}^{\mathsf{T}} p \geq -\|p\|_2$. As a result, the `else` implicationx can be written as:

$$f_R(p) = -1 - \hat{x}_{\mathcal{L}}^{\mathsf{T}} p \|p\|_2^{-1}. \tag{27}$$

We can now use (26) and (27) directly in (23), which yields a smooth approximation of the approach cone constraint:

$$\cos(\theta_{\text{appch}}) - \big(1 + \cos(\theta_{\text{appch}})\big) \tilde{R}_\kappa^{\text{appch}}(p) - \hat{x}_{\mathcal{L}}^{\mathsf{T}} p \|p\|_2^{-1} \leq 0. \tag{28}$$

D. Modeling Plume Impingement

The plume impingement constraint (12g) is modeled in a very similar way. Recall that the rendezvous trajectory has N_c control opportunities and the chaser has $\mathcal{I}_{\text{fr}}$ forward-facing thrusters. Let us focus on the k-th control opportunity for thruster $i \in \mathcal{I}_{\text{fr}}$. Comparing (12g) with (14a), we have $n_g = 1$ and $z = \big[p(k't_c); \Delta t_{ik}\big]$. The predicate takes after (25):

$$g_1\big(p(k't_c)\big) = p(k't_c)^{\mathsf{T}} p(k't_c) - r_{\text{plume}}^2, \tag{29}$$

This predicate is then used in (22) to form $\tilde{R}_\kappa^{\text{plume}}$, the smooth `or` approximation for the plume impingement predicate. The `if` implication for plume impingement is an equality constraint, whereas our standard formulation (14) requires an inequality. To reconcile the two situations, one possible approach is to leverage (12f) and to realize that $\Delta t_{ik} \in [0, \Delta t_{\max}]$. Thus, we can impose the constraint:

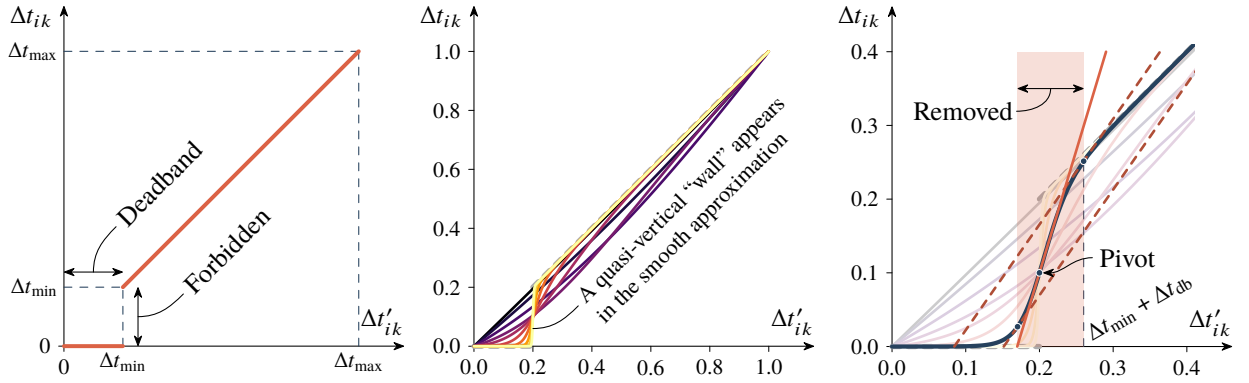
$$0 \leq \Delta t_{ik} \leq \Delta t_{\max}, \tag{30}$$

and we can write the following `if` implication:

$$f_L(\Delta t_{ik}) = \Delta t_{ik}. \tag{31}$$

Equation (31) together with (30) enforce $0 \leq \Delta t_{ik} \leq 0$ when the predicate (29) is `true`, which is equivalent to (12g). When the chaser is outside of the plume impingement sphere, the forward-facing thrusters are free to fire. We can express this as the following `else` implication:

$$f_R(\Delta t_{ik}) = \Delta t_{ik} - \Delta t_{\max}. \tag{32}$$



(a) Exact deadband curve. **(b) Deadband approximation using (23).** **(c) Zoomed-in view of (b) around $\Delta t_{\min}$.**

Fig. 9 Approximation of the MIB constraint (12f) using multinomial logit smoothing (23).

Equations (31) and (32) can now be substituted into (23), yielding a smooth approximation of the plume impingement constraint:

$$\Delta t_{ik} \leq \tilde{R}_{\kappa}^{\text{plume}}\big(p(k't_c)\big)\Delta t_{\max}. \tag{33}$$

E. Modeling the Minimum Impulse Bit

The MIB constraint (12f) is the most intricate one to model effectively, and has been the core motivation behind developing a new way to handle discrete logic constraints. Our past work used STCs, which exhibited locking and prevented the algorithm from converging effectively in some cases [26]. Among the several possible ways of fitting the MIB constraint into the discrete logic framework of (14), we present one way that yields good convergence performance across a wide variety of instances of Problem 12.

Let us focus the discussion on pulse Δt_{ik}, in other words the i-th thruster at the k-th control opportunity. We view the thruster as an actuator with a deadband, as illustrated in Figure 9a. The "input" or "reference" pulse duration is given by a *continuous* variable $\Delta t'_{ik} \in [0, \Delta t_{\max}]$. When this value falls below $\Delta t_{\min}$, the "obtained" or "output" pulse duration which the thruster actually executes is zero. Thus, while $\Delta t'_{ik}$ is a continuous variable that can take any value in $[0, \Delta t_{\max}]$, the obtained pulse duration Δt_{ik} exhibits a jump discontinuity at $\Delta t_{\min}$. Modeling this jump discontinuity is precisely the focus of our smooth approximation strategy.

Comparing Figure 9a with the standard model (14), we can write the following `if-else` logic:

$$\Delta t'_{ik} \leq \Delta t_{\min} \implies \Delta t_{ik} = 0, \tag{34a}$$

$$\Delta t'_{ik} > \Delta t_{\min} \implies \Delta t_{ik} = \Delta t'_{ik}. \tag{34b}$$

We can thus define $n_g = 1$, $z = \left[\Delta t_{ik}; \Delta t'_{ik}\right]$, and use the predicate:

$$g_1(\Delta t'_{ik}) = \Delta t'_{ik} - \Delta t_{\min}. \tag{35}$$

This predicate is used in (22) to form $\tilde{R}^{\text{mib}}_{\kappa}$, the smooth `or` approximation for the MIB predicate. As for the implications on the right-hand side of (34), we can use pairs of inequalities to represent equality constraints as required by (14). This yields the following `if` and `else` implications:

$$f_L(\Delta t_{ik}) = \begin{bmatrix} \Delta t_{ik} \\ -\Delta t_{ik} \end{bmatrix}, \quad f_R(\Delta t_{ik}, \Delta t'_{ik}) = \begin{bmatrix} \Delta t_{ik} - \Delta t'_{ik} \\ \Delta t'_{ik} - \Delta t_{ik} \end{bmatrix}. \tag{36}$$

Just like for the approach cone and plume impingement constraints, (36) can now be substituted into (23) to obtain a smooth approximation of the deadband behavior in Figure 9a. Simplifying the result, we obtain the following constraint:

$$\Delta t_{ik} = \tilde{R}^{\text{mib}}_{\kappa}(\Delta t'_{ik})\Delta t'_{ik}. \tag{37}$$

The smooth approximation is shown in Figure 9b for a number of homotopy parameter κ values. We call this approximation the smooth deadband curve (SDC). As κ increases, the approximation converges to the exact deadband curve *with one significant exception*: the "forbidden" region (i.e., the jump discontinuity) from Figure 9a becomes part of the SDC as a quasi-vertical "wall" for large κ in Figure 9b. This raises the followig question: can a rendezvous trajectory exploit this wall and therefore "get around" the MIB constraint? Alas, the answer is yes, and our numerical tests show that this happens quite regularly. Generally, this adversarial exploitation of the model feeds into a long-standing pain point of optimization. As Betts writes in [54, p. 701], "If there is a flaw in the problem formulation, the optimization algorithm will find it." To fix this side effect and forbid Δt_{ik} from exploiting the wall, we introduce a new constraint to the optimization problem.

1. The Wall Avoidance Constraint

We now develop an extra constraint to ensure that no Δt_{ik} can exploit the wall part of the SDC (37). We ask ourselves the following question: what makes the wall different from the other parts of the SDC? One property stands out above all others: for large κ values the wall has a very large gradient, as opposed to other parts of the curve where the gradient is approximately zero or one. There is another favorable property of (37): in the limit as κ increases, the smooth approximation converges to a function whose gradient monotonically increases for $\Delta t_{ik} \in [0, \Delta t_{\min})$, and monotonically decreases for $\Delta t_{ik} \in (\Delta t_{\min}, \Delta t_{\max}]$. In other words, (37) has an *inflection point* at $\Delta t_{\min}$ for large κ, where its gradient takes its maximum value. We call this the "pivot" since the SDC appears to revolve around this point as κ increases. This is visible in Figures 9b and 9c for the brighter colored curves that correspond to larger κ values.

We develop the following intuition from the above discussion: if we constrain Δt_{ik} such that the SDC's gradient is sufficiently less than its value at the pivot, then Δt_{ik} cannot exploit the wall. To put this into practice, define Δt_{db} to be a "buffer" around $\Delta t_{\min}$. We want the gradient at Δt_{ik} to be less than its value at the buffered pulse duration $\Delta t_{\min} + \Delta t_{\text{db}}$. The SDC gradient at $\Delta t_{\min} + \Delta t_{\text{db}}$ is computed as follows using (37):

$$G_{\text{db},\kappa} \triangleq \left.\frac{\mathrm{d}\tilde{R}_{\kappa}^{\text{mib}}(\Delta t'_{ik})}{\mathrm{d}\Delta t'_{ik}}\right|_{\Delta t'_{ik}=\Delta t_{\min}+\Delta t_{\text{db}}} (\Delta t_{\min} + \Delta t_{\text{db}}) + \tilde{R}_{\kappa}^{\text{mib}}(\Delta t_{\min} + \Delta t_{\text{db}}). \tag{38}$$

This allows us to impose the following *wall avoidance constraint*, which prevents Δt_{ik} from taking values along the wall of the SDC:

$$\frac{\mathrm{d}\tilde{R}_{\kappa}^{\text{mib}}(\Delta t'_{ik})}{\mathrm{d}\Delta t'_{ik}}\Delta t'_{ik} + \tilde{R}_{\kappa}(\Delta t'_{ik}) \leq G_{\text{db},\kappa}. \tag{39}$$

Figure 9c illustrates an example region of $\Delta t'_{ik}$ and Δt_{ik} values that is effectively removed by (39). In the figure, $\Delta t_{\min} = 0.2$ s and $\Delta t_{\text{db}} = 0.06$ s. The gradients of all points inside the red region are larger than $G_{\text{db},\kappa}$, hence the corresponding choices of Δt_{ik} are infeasible. Because the aforementioned monotonicity property guarantees that this region contains the wall, the net effect is that the SDC wall can no longer be exploited by the optimization.

2. Improving Convergence

The smoothed MIB constraint (37) introduced a new input variable $\Delta t'_{ik}$ to represent a reference pulse duration. This variable was necessary to model the deadband curve in Figure 9a. If we compare the deadband curve to the original MIB constraint (12f), we realize that the only "useful" parts of the curve in Figure 9a that we actually need are the origin (i.e., $[\Delta t_{ik}; \Delta t'_{ik}] = 0$) and the continuous trace $\Delta t_{ik} = \Delta t'_{ik}$ where $\Delta t_{ik} > \Delta t_{\min}$. In both cases, we have the simple relationship $\Delta t_{ik} = \Delta t'_{ik}$. Our numerical experience shows that encouraging this equality significantly improves the convergence process of the algorithm in Section IV. We do this by adding the following regularization term to the original cost (12a):

$$J_{\text{eq}} = w_{\text{eq}} \Delta t_{\min}^{-1} \sum_{i=1}^{n_{\text{rcs}}} \sum_{k=1}^{N_c} \|\Delta t_{ik} - \Delta t'_{ik}\|_1, \tag{40}$$

where $w_{\text{eq}} > 0$ is some small weight for the cost. We view (40) as penalizing the choice $\Delta t_{ik} \neq \Delta t'_{ik}$. The use of the one-norm encourages sparsity in the number of Δt_{ik} that violate the equality. This choice traces back to theory from lasso regression, sparse signal recovery, and basis pursuit to compute sparse solutions via one-norm regularization [41].

F. Smoothed Rendezvous Problem

We are now in a position to restate Problem 12 as a continuous optimization problem by using the smoothed discrete logic constraints from the previous sections. The process is straightforward: simply replace each discrete logic constraint

with its smooth approximation. We call the result the smooth rendezvous problem (SRP), stated below.

$$\min_{x,\Delta t,\Delta t',t_f} J_{\text{fuel}} + J_{\text{eq}} \tag{41a}$$

$$\text{s.t. Dynamics (12b)-(12e)}, \tag{41b}$$

$$0 \le \Delta t_{ik} \le \Delta t_{\max},\ 0 \le \Delta t'_{ik} \le \Delta t_{\max}, \tag{41c}$$

$$\Delta t_{ik} = \tilde{R}^{\text{mib}}_{\kappa}(\Delta t'_{ik})\Delta t'_{ik}, \tag{41d}$$

$$\frac{\mathrm{d}\tilde{R}^{\text{mib}}_{\kappa}(\Delta t'_{ik})}{\mathrm{d}\Delta t'_{ik}}\Delta t'_{ik} + \tilde{R}_{\kappa}(\Delta t'_{ik}) \le G_{\text{db},\kappa}, \tag{41e}$$

$$\Delta t_{ik} \le \tilde{R}^{\text{plume}}_{\kappa}\big(p(k't_c)\big)\Delta t_{\max} \text{ for all } i \in \mathcal{I}_{\text{fr}}, \tag{41f}$$

$$\cos(\theta_{\text{appch}}) - \big(1 + \cos(\theta_{\text{appch}})\big)\tilde{R}^{\text{appch}}_{\kappa}(p) - \hat{x}^{\mathsf{T}}_{\mathcal{L}} p \|p\|_2^{-1} \le 0, \tag{41g}$$

$$\text{Boundary conditions (12i)-(12k)}. \tag{41h}$$

The key difference between Problem 12 and the new Problem 41 is that the latter no longer contains integer variables to solve. Instead, there is a single homotopy parameter κ that regulates how accurately the smoothed constraints (41d), (41f), and (41g) approximate the original discrete logic. Thus, we have eliminated the third difficulty mentioned in Section II.F (i.e., the mixed-integer programming aspect). However, we are now faced with solving a nonconvex optimization problem, and there remains the question of how to set the value of κ. In the next section we answer both questions using sequential convex programming and numerical continuation.

IV. Sequential Convex Programming with Numerical Continuation

We now present a numerical optimization algorithm that solves Problem 41. This algorithm combines two key methodologies: sequential convex programming (SCP) and numerical continuationg. SCP is an iterative scheme designed to solve Problem 41 for a given value of κ. The *raison d'être* for numerical continuation is to greatly expand the region of convergence of iterative schemes [55]. Due to the vanishing gradient problem and the very large gradients at the "step" transition points of discrete logic (see, for example, Figures 7, 8, and 9), SCP is unlikely to converge if a large κ value is used right away together with an initial guess that is not already almost optimal [9]. As a result, numerical continuation is used to aid SCP convergence. This is done by providing an algorithm to update κ starting from a small value where the smooth approximation is coarse, and increasing it until a large value where the approximation attains the accuracy level requested by the user.

Our core contribution is to *merge* these two methods. In other words, the algorithm that we present is not SCP with a numerical continuation "outer loop". Rather, the methods are run simultaneously, which is a novel feature of the proposed algorithm. The numerical results in Section V show that this can dramatically decrease the total number of

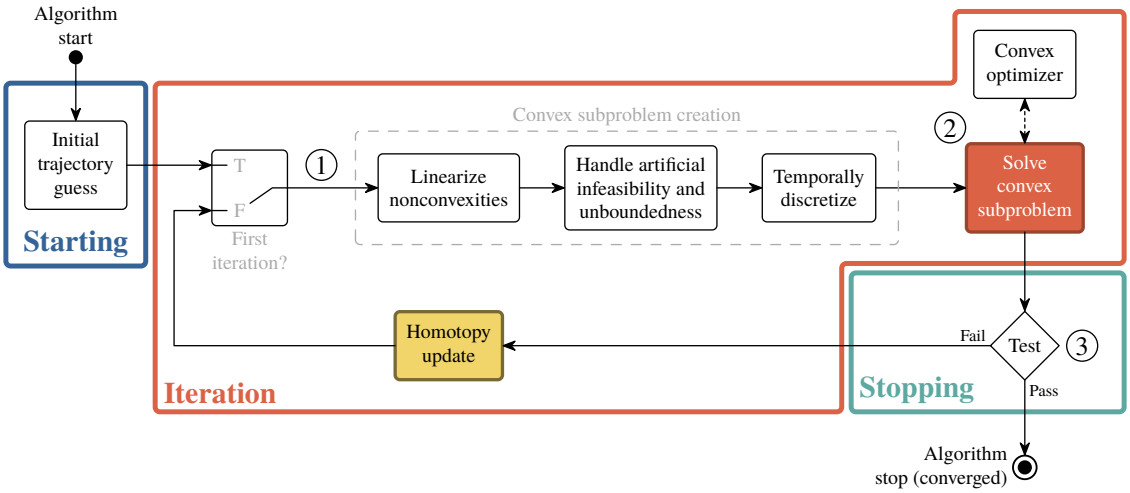


Fig. 10 Block diagram illustration of the PTR sequential convex programming algorithm. Our novel contribution is the "homotopy update" block that implements numerical continuation to solve Problem 41.

required iterations without sacrificing optimality.

A. The Penalized Trust Region Algorithm

We begin by describing the penalized trust region (PTR) algorithm. This is a particular SCP method that has been widely used for fast and even real-time solution of nonconvex problems like Problem 41, where the value of κ is fixed [27, 29, 52]. This section provides a brief overview of PTR and identifies locations where the method is changed in order to embed numerical continuation. These changes are then described in the sections that follow. For the standard portions of the PTR algorithm, we will refer the reader to existing literature which already provides detailed explanations.

The goal of SCP in general, and PTR in particular, is to solve continuous-time optimal control problems of the following form:

$$\min_{x,u,p,t_f} \; J(x,u,p) \tag{42a}$$

$$\text{s.t. } \dot{x}(t) = f\big(t, x(t), u(t), p\big), \tag{42b}$$

$$\big(x(t), p\big) \in \mathcal{X}(t), \;\; \big(u(t), p\big) \in \mathcal{U}(t), \tag{42c}$$

$$s\big(t, x(t), u(t), p\big) \leq 0, \tag{42d}$$

$$g_{\text{ic}}\big(x(0), p\big) = 0, \;\; g_{\text{tc}}\big(x(t_f), p\big) = 0, \tag{42e}$$

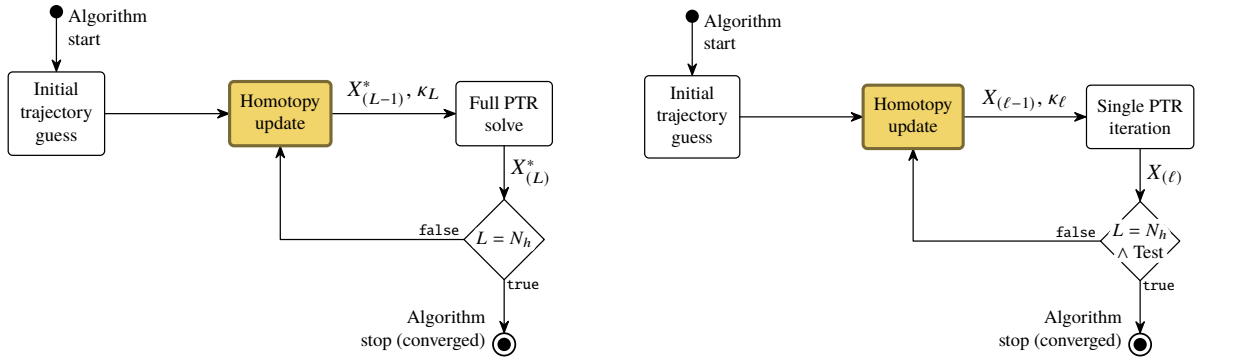
where $x(\cdot) \in \mathbb{R}^{n_x}$ is the state trajectory, $u(\cdot) \in \mathbb{R}^{n_u}$ is the control trajectory, and $p \in \mathbb{R}^{n_p}$ is a vector of parameters. The function $f : \mathbb{R} \times \mathbb{R}^{n_x} \times \mathbb{R}^{n_u} \times \mathbb{R}^{n_p} \to \mathbb{R}^{n_x}$ encodes the nonlinear equations of motion, which are assumed to be at least once continuously differentiable. Initial and terminal boundary conditions are enforced by using the continuously differentiable functions $g_{\text{ic}} : \mathbb{R}^{n_x} \times \mathbb{R}^{n_p} \to \mathbb{R}^{n_{\text{ic}}}$ and $g_{\text{tc}} : \mathbb{R}^{n_x} \times \mathbb{R}^{n_p} \to \mathbb{R}^{n_{\text{tc}}}$. The convex and nonconvex path (i.e., state

and control) constraints are imposed using the convex sets $\mathcal{X}(t)$, $\mathcal{U}(t)$, and the continuously differentiable function $s : \mathbb{R} \times \mathbb{R}^{n_x} \times \mathbb{R}^{n_u} \times \mathbb{R}^{n_p} \to \mathbb{R}^{n_s}$. Finally, a continuously differentiable cost function $J : \mathbb{R}^{n_x} \times \mathbb{R}^{n_u} \times \mathbb{R}^{n_p} \to \mathbb{R}$ encodes some trajectory property that is to be minimized. Without giving the explicit details here, we note that Problem 41 can be fit into the mold of Problem 42 for any fixed value of κ. The interested reader may consult our open-source implementation for details [8], and may refer to [9] for a broad tutorial on the modeling process.

At the core of PTR is the idea of solving Problem 42 through iterative convex approximation. The algorithm can be represented in block diagram form as shown in Figure 10. The method is composed of three major parts: a way to guess the initial trajectory (Starting), an iteration scheme that refines the trajectory until it is feasible and locally optimal (Iteration), and an exit criterion to stop once a trajectory has been computed (Stopping). Strictly speaking, PTR is a nonlinear local optimization algorithm known as a trust region method [42, 56, 57].

Let us begin by assuming that the homotopy parameter κ is fixed to a specific value. In other words, the "homotopy update" block in Figure 10 is a simple feed-through that does nothing. PTR solves Problem 41 using a sequence of convex approximations called *subproblems*. Roughly speaking, the convex approximation is improved each time that a new solution is obtained. Going around the loop of Figure 10, all algorithms start with a user-supplied initial guess, which can be very coarse (more on this later). At ①, the SCP algorithm has available a so-called reference trajectory, which may be infeasible with respect to the problem dynamics and constraints. The nonconvexities of the problem are removed by a local linearization around the reference trajectory, while convex parts of the problem are kept unchanged. To ensure that linearization does not cause the subproblems to become infeasible, extra terms are added which are known as virtual controls (for the dynamics (42b)) and virtual buffers (for the constraints (42d) and (42e)). The resulting convex continuous-time subproblem is temporally discretized to yield a finite-dimensional convex optimization problem. The optimal solution to the discretized subproblem is computed at ②, where the SCP algorithm makes a call to any appropriate convex optimization solver. The solution is tested at ③ against stopping criteria. If the test passes, the algorithm has converged and the most recent solution from ② is returned. Otherwise, the solution becomes the new reference trajectory for the next iteration of the algorithm.

The traditional PTR method as described above is covered in great depth in existing literature. We refer the reader to a recent expansive tutorial [9], and to papers which describe PTR in the context of rocket landing, rendezvous and docking, and quadrotor flight [25–29, 52]. In this paper we will focus our attention on the novel "homotopy update" block in Figure 10. This block implements a numerical continuation method in order to update κ until the smooth approximations of discrete logic from Section III become quasi-exact (in other words, accurate to within a user-defined tolerance that can be arbitrarily small).



(a) The non-embedded approach, where each homotopy update is followed by a full PTR solve.

(b) The proposed embedded approach, where homotopy updates occur between individual PTR iterations.

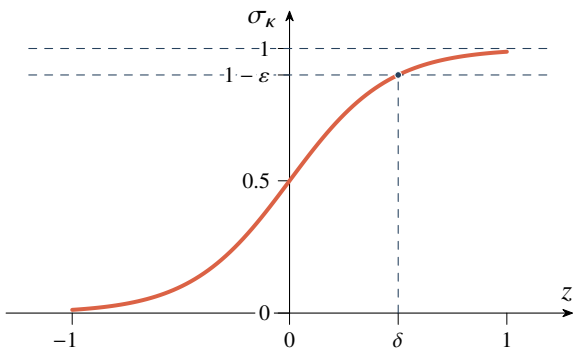
Fig. 11 Comparison of the standard and embedded numerical continuation schemes. The "Test" in (b) corresponds to the stopping criterion from Figure 10.

B. Non-embedded Numerical Continuation

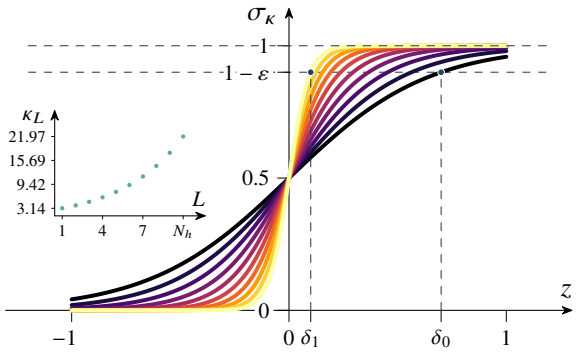
In order to arrive at the embedded numerical continuation approach, we begin by motivating a non-embedded scheme which we will then generalize to the embedded algorithm. As shown in Figure 11a, the basic idea is to update the homotopy parameter κ after each time that Problem 41 is solved for the current value of κ. Furthermore, each new call to PTR is "warm started" by providing the most recent solution as the initial guess in Figure 10.

In formal terms, let L denote the iteration number of the non-embedded algorithm. Effectively, L corresponds to the number of full PTR solves of Problem 41 that have occured up until the end of that iteration. If we place ourselves at iteration L, then let κ_L denote the homotopy parameter chosen by the "homotopy update" block, and let $X^*_{(L)}$ be the corresponding solution of Problem 41 computed by PTR. Importantly, PTR is warm started with the initial guess $X^*_{(L-1)}$. When $L > 1$, this corresponds to the PTR solution from the previous iteration (i.e., the solution of Problem 41 for the previous value of κ). For the first iteration $L = 1$, $X^*_{(0)}$ corresponds to the user-chosen initial trajectory guess. The job of the homotopy update is the following: compute κ_L given $X^*_{(L-1)}$ and κ_{L-1}. While we describe the details below, the basic idea is as follows: κ_L grows with L and, eventually, the smooth approximations from Section III become quasi-exact representations of the original discrete logic (e.g., see the example in Figure 7). Once κ_L reaches some large user-defined value that yields an accurate enough approximation of the discrete logic, the algorithm terminates.

The remaining task for the non-embedded numerical continuation approach is to define the internals of the homotopy update block in Figure 11a. Our method stems from viewing the sigmoid function (20) as a smooth model for a step function. As we increase the homotopy parameter κ, we want to explicitly control how "sharply" the sigmoid approximates the step function's discontinuity. This leads us to the following update rule, which is illustrated in Figure 12. As shown in Figure 12a, we define two parameters: a *precision* $\varepsilon \in (0, 1)$ and a *smoothness* $\delta > 0$. The sigmoid function σ_κ in (20) is then required to satisfiy the following *interpolation condition*: it must equal $1 - \varepsilon$ when its argument equals δ. An exact step function corresponds to $\varepsilon = 0$ and $\delta = 0$, so we view ε and δ as defining how much



(a) Each sigmoid is formed by fixing the values of ε and δ, which determine the homotopy parameter κ.



(b) The smoothness parameter δ is decreased from δ_0 to δ_1. The sigmoid is sharpened as a result.

Fig. 12 The homotopy parameter κ is updated by fixing a *precision* ε and gradually reducing the *smoothness* δ where the sigmoid attains the value $1-\varepsilon$.

the sigmoid deviates from the exact step function.

For the homotopy update rule, we hold ε constant and define two bounds on δ: a "smoothest" value δ_0 and a "sharpest" value $\delta_1 < \delta_0$. We then sweep δ according to a geometric progression:

$$\delta_\alpha = \rho^\alpha \delta_0, \qquad \rho = \delta_1/\delta_0, \tag{43}$$

where $\alpha \in [0,1]$ is an interpolation parameter. The effect is that the sigmoid function is sharpened, as shown in Figure 12b. The homotopy value that satisfies the interpolation condition is given by:

$$\kappa_\alpha = \frac{\ln\left(\varepsilon^{-1}-1\right)}{\rho^\alpha \delta_0}. \tag{44}$$

Equation (44) defines a continuous range of homotopy values from the smoothest ($\alpha = 0$) to the sharpest ($\alpha = 1$) case. In practice, we set a fixed number of updates N_h and let $\alpha = (L-1)/(N_h-1)$ for $L = 1, 2, \ldots, N_h$. Thus, N_h defines the number of iterations in the non-embedded numerical continuation algorithm of Figure 11a. By substituting this expression for α into (44), we obtain the following formula for the homotopy value κ_L at iteration L:

$$\kappa_L = \frac{\ln\left(\varepsilon^{-1}-1\right)}{\rho^{(L-1)/(N_h-1)}\delta_0}. \tag{45}$$

C. Embedded Numerical Continuation

We are now ready to describe the embedded numerical continuation algorithm shown in Figure 11b. One key difference distinguishes this algorithm from the non-embedded approach: PTR does not have to run to completion before the homotopy parameter κ is increased. As shown in Figure 11b, the full PTR solve of the non-embedded method

is replaced by a *single* PTR iteration (which corresponds to the top half of the PTR block diagram in Figure 10). We use ℓ to denote the PTR iteration counter. At each iteration ℓ, a homotopy update rule is called that potentially changes the value of κ. This new value and the most recent PTR iterate (i.e., subproblem solution) are used for the next PTR iteration. The process shown in Figure 11b works exactly like in Figure 10, with the blocks rearranged.

Now that we understand how the algorithm is structured, we need to describe the homotopy update. This is composed of two parts: deciding *whether* to update κ, and then updating it. The latter piece works just like in the previous section. Once we know that κ should be updated, we use (46) to compute its new value:

$$\kappa_\ell = \frac{\ln\left(\varepsilon^{-1} - 1\right)}{\rho^{L/(N_h-1)}\delta_0}, \quad L \leftarrow L + 1, \tag{46}$$

where L now represents the number of times that the homotopy parameter has been updated so far (the count starts at $L = 0$). The core of the embedded homotopy update rule is the first piece: deciding whether to update κ. For this, let J_ℓ denote the subproblem cost achieved at PTR iteration ℓ. If the following condition holds, then we update κ:

$$\beta_{\text{worse}} \leq \frac{J_{\ell-1} - J_\ell}{|J_{\ell-1}|} \leq \beta_{\text{trig}} \quad \wedge \quad L < N_h. \tag{47}$$

The second half of the condition is simple: don't update κ if this is already its highest value. The first half is a condition on relative cost decrease over the past iteration. If the cost in the current iteration decreased by less than β_{trig} relative to the last iteration, then the algorithm is "converging" for the current value of κ and it is time to update it. However, the cost is not guaranteed to decrease monotonically with PTR iterations. Thus, the relative cost decrease may be negative, which means that the cost increased over the past iteration. In this case, we may specify a certain (small) tolerance $\beta_{\text{worse}} < 0$. This means that we will still update κ if the cost did not increase by more than β_{worse} allows. In the numerical results of Section V we set $\beta_{\text{worse}} = -10^{-3}$ (i.e., a 0.1% tolerance).

Algorithm 1 The proposed sequential convex programming algorithm with embedded numerical continuation. The method can solve optimal control problems with discrete logic constraints.

1: $X_{(0)} \leftarrow$ initial trajectory guess, $L \leftarrow 0$, $\ell \leftarrow 0$
2: **while** `true` **do**
3: $\quad \ell \leftarrow \ell + 1$
4: $\quad$ **if** $\ell = 1$ or (47) is `true` **then**
5: $\quad\quad$ Execute the update rule (46)
6: $\quad$ **else**
7: $\quad\quad \kappa_\ell \leftarrow \kappa_{\ell-1}$
8: $\quad X_{(\ell)} \leftarrow$ do one PTR step (see Figure 10) using κ_ℓ and the reference trajectory $X_{(\ell-1)}$
9: $\quad$ **if** $L = N_h$ and $X_{(\ell)}$ passes the Test at location ③ in Figure 10 **then**
10: $\quad\quad$ **return** $X_{(\ell)}$ ▷ Converged

To summarize the above discussion, Algorithm 1 formalizes the embedded numerical continuation scheme illustrated in Figure 11b. On lines 4-7 of Algorithm 1, which correspond to the "homotopy update" block of Figure 11b, a

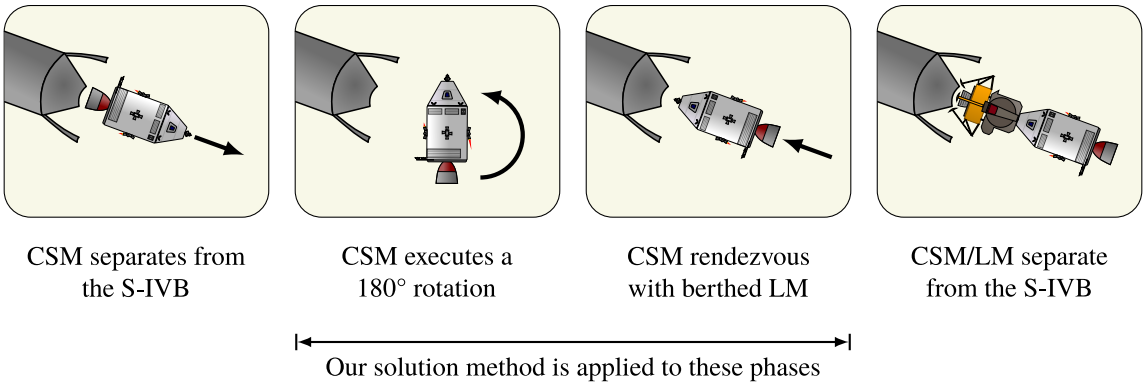


Fig. 13 Illustration of the Apollo CSM Transposition and Docking maneuver with the LM housed inside the Saturn S-IVB third stage [35, Figure 2-11].

decision is made using (47) whether to update the current κ value. If the answer is `true`, then κ is updated using (46). Otherwise, it is maintained at its present value. The algorithm iterates in this way until the stopping criterion on line 9 of Algorithm 1 is satisfied.

V. Numerical Results

In this section we apply our solution method to a more challenging variant of the historical docking maneuver between the Apollo Command and Service Module (CSM) and the Lunar Module (LM). Section V.A defines the problem parameters and Section V.B discusses the solved trajectory and various computational aspects. The key takeaways are as follows. Our algorithm is able to consistently find rendezvous trajectories that satisfy the discrete logic constraints from Section II. The algorithm is insensitive to the β_{trig} tolerance parameter in (47), and in fact increasing this value can dramatically reduce the total number of iterations. The total convex solver time is approximately 13.5 s, which is fast for an implementation that is not optimized for speed. Section V.B discusses how the algorithm can be made to run in under 10 s of total solution time.

A. Problem Parameters

The numerical example is inspired by the Apollo CSM "Transposition and Docking" (TD) maneuver [40, Section 2.13.1.1]. As illustrated in Figure 13, this maneuver uses the RCS thrusters of the CSM in order to dock with the LM, which is housed inside the Saturn S-IVB third stage. The most interesting feature of this maneuver is the 180° rotation of the CSM, which allows us to stress-test our solution method for the CSM's coupled translation and rotation dynamics from Section II.A.

The SM RCS system is composed of four similar, independent "quads" located 90° apart around the Service Module (SM) circumference, as illustrated in Figure 14. Each quad is composed of four independent hypergolic pressure-fed pulse-modulated thrusters, yielding a total of $n_{\text{rcs}} = 16$ control inputs [40, Section 2.5.1]. We model the complete, high-

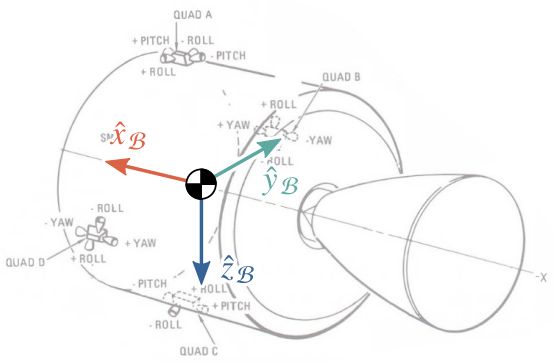


Fig. 14 Layout of the Apollo SM RCS thrusters [40, Figure 2.5-1]. There are $n_{\text{rcs}} = 16$ thrusters grouped into four "quads" labeled A/B/C/D and each having four independent hypergolic pressure-fed thrusters.

fidelity CSM geometry according to public NASA documentation [35, 40]. The CSM mass and inertia are specified in [35, Table 3.1-2]:

$$m \approx 30323 \text{ kg}, \quad J \approx \begin{bmatrix} 49249 & 2862 & -370 \\ 2862 & 108514 & -3075 \\ -370 & -3075 & 110772 \end{bmatrix} \text{ kg m}^2. \tag{48}$$

The RCS thrusters are capable of producing approximately $\|\hat{f}_i\|_2 = 445$ N of thrust in steady-state operation [40, Figure 2.5-8, Table 4.3-1]. However, during transposition and docking they are pulse-fired in bursts [39, 40, Section 2.5.1]. In this mode of operation, the minimum electric on-off pulse width is 12 ms [40, Section 2.5.2.3.1], generating an irregular burst of thrust that lasts for upwards of 65 ms and with a peak of 300 to 350 N [40, Figure 2.5-9]. To buffer the thrust away from this irregular region, we set $\Delta t_{\min} = 112$ ms (which corresponds to a 50 N s impulse) and $\Delta t_{\max} = 1$ s. On a system architecture level, we assume that irregularity in the thrust profile is going be corrected by a feedback control system that tracks our open-loop rendezvous trajectory.

Table 1 summarizes the major numerical values used to obtain the results of the following section. Other parameters not mentioned (such as the CSM geometry) can be consulted directly in our open-source implementation [8]. Note that the maneuver we are seeking to optimize is more complicated than the original Apollo TD concept of operations. The Apollo initial position p_0 was almost purely along the $\hat{x}_{\mathcal{L}}$ axis, whereas we add significant $\hat{y}_{\mathcal{L}}$ and $\hat{z}_{\mathcal{L}}$ displacement in order to stress the algorithm. Furthermore, the original TD maneuver takes place after translunar injection whereas we assume a circular lower Earth orbit. This allows us to use the Clohessy-Wiltshire-Hill dynamics (2), which adds further complexity compared to our previous work [26].

Our algorithm from Section IV is implemented using the framework introduced in [9]. The Julia programming language is used because it is simple to read like Python, yet it can be as fast as C/C++ [58]. The timing results in the next section correspond to a Dell XPS 13 9260 laptop powered by an Intel Core i5-7200U CPU clocked at 2.5 GHz. The computer has 8 GiB LPDD3 RAM and 128 KiB L1, 512 KiB L2, and 3 MiB L3 cache. The ECOS software (written in

Parameter	Value
$\Delta t_{\min}$	112 ms
$\Delta t_{\max}$	1 s
F_{rcs}	445 N
r_{plume}	20 m
r_{appch}	30 m
θ_{appch}	10°
t_f	$\in [100, 1000]$ s
n_o	400 km LEO
p_0	$100\hat{x}_{\mathcal{L}} - 20\hat{z}_{\mathcal{L}} + 20\hat{y}_{\mathcal{L}}$ m
v_0	0 m s^{-1}
q_0	$[0; 0; 0; 1]$
$\omega_0,\ \omega_f$	0 rad s^{-1}
p_f	$4.48\hat{x}_{\mathcal{L}} - 0.05\hat{y}_{\mathcal{L}} + 0.17\hat{z}_{\mathcal{L}}$ m
v_f	$-0.1\hat{x}_{\mathcal{L}}$ m s^{-1}
q_f	$[0; 0.26; 0.97; 0]$
ε_{r_f}	0.1 m
ε_{v_f}	1 cm s^{-1}
ε_{q_f}	1°
ε_{ω_f}	0.01° s^{-1}

(a) Rendezvous parameters.

Parameter	Value
ε	10^{-2}
δ_0	10
δ_1	0.01
N_h	10
w_{eq}	1
β_{worse}	-10^{-3}
β_{trig}	0.1
Δt_{db}	11.2 ms

(b) Algorithm parameters.

Table 1 Numerical parameters for the Apollo CSM/LM Transposition and Docking trajectory.

C) is used as the low-level numerical convex solver at location ② in Figure 10 [59].

B. Computed Trajectory

Figures 15-19 exhibit our algorithm's solution as well as its associated properties for Problem 41 with the parameters in Table 1. The initial guess provided to the algorithm in Figure 10 is a straight-line interpolation in position and a spherical linear interpolation for the attitude quaternion [37]. The initial RCS thruster pulse durations are all set to zero.

We begin by discussing the position trajectory, which is shown in the LVLH frame in the left column of Figure 15. Projections are also shown for the approach sphere (blue), the approach cone (green), and the plume impingement sphere (red). The red vectors represent the direction and relative magnitude of the net thrust generated by the combined action of the RCS thrusters. The circular markers show the chaser's COM for the discrete-time solution, while the continuous trajectory is obtained by integrating the optimal control through the original nonlinear dynamics of Section II.A. Because the two trajectories coincide, we conclude that the converged trajectory is dynamically feasible.

The trajectory in Figure 15 has two salient features. First, the RCS thrusters fire mostly at the start to initiate motion, and near the end to cancel vehicle rates just prior to docking. This resembles the classical two-impulse rendezvous maneuver [36], modified to account for 6-DOF dynamics, the RCS system geometry, and the discrete logic constraints

(41c)-(41g), all of which are absent in the classical setup. Secondly, recall that negative $\hat{z}_{\mathcal{L}}$ positions correspond to lower orbits where objects move faster relative to the target. The chaser exploits this "gift" from orbital mechanics by dipping into the negative $\hat{z}_{\mathcal{L}}$ positions (see the top and bottom plots) where it benefits from a zero-fuel acceleration to the target. Furthermore, note how the chaser stays within the approach cone when it is inside the approach sphere, as required by (41g).

The evolution of the chaser's attitude along this trajectory is shown in the right column of Figure 15. The quaternion attitude was converted to the more informative Euler angles using the Tait-Bryan yaw-pitch-roll convention. Green vertical lines demarcate the times at which the chaser enters the approach and plume imbpingement spheres. Velocity and angular rate states exhibit jumps according to our impulsive thruster model in Section II.B. Note that the chaser assumes a 30° roll angle at docking, as required by the CSM/LM geometry [35, Figure 2-4].

The RCS thruster pulse history is shown in Figure 16 for quad D from Figure 14, which is representative of the pulse histories for the other quads. The pulses are relatively sparse and clustered around the start and end of the trajectory. As required by the plume impingement constraint (41f), the forward thrusters are silent once the chaser is inside the plume impingement sphere. Furthermore, some pulse durations are almost exactly $\approx \Delta t_{\min}$ s. This shows that the smoothed discrete logic (41d) actively enforces the MIB constraint (5). The constraint (41d) is indispensable for satisfying the minimum impulse-bit, and removing it causes the MIB constraint to be violated.

We can estimate the total fuel consumption of the rendezvous trajectory using NASA charts for RCS thruster performance [38, Figure 4.3-6 and 4.3-7]. These charts map pulse duration to the corresponding amount of fuel consumed by a single thruster. By applying these charts to the pulse history in Figure 16, we obtain a fuel consumption of 2.63 kg. Unfortunately, NASA documentation on the actual fuel consumption achieved by the Apollo missions is unclear; [35, Table 3.1-7] suggests that it was 32 kg, but this confounds the other phases of the TD maneuver which we do not consider (see Figure 13). In any case, it appears that our trajectory uses considerably less fuel, not to mention that its initial conditions are more challenging than those of the Apollo concept of operations due to the initial position offsets along $\hat{y}_{\mathcal{L}}$ and $\hat{z}_{\mathcal{L}}$.

The convergence process of our algorithm and the runtime performance of its implementation are shown in Figure 17. Formulate measures the time taken to parse the subproblem into the input format of the convex optimizer; Solve measures the time taken by the core convex numerical optimizer; Discretize measures the time taken to temporally discretize the linearized dynamics from Section II.A; and Overhead measures the time taken by all other supporting tasks during a single PTR iteration.

The algorithm appears to attain a superlinear convergence rate (noticeable over iterations $\ell \in [19, 30]$). A small spike in solver time appears around the iterations where the homotopy parameter changes rapidly (see Figure 18 ahead). Otherwise, the subproblem difficulty stays roughly constant over the iterations. While our Julia implementation takes a median time of 50 s, the cumulative median time for solving the subproblems at location ② in Figure 10 is 13.5 s (which

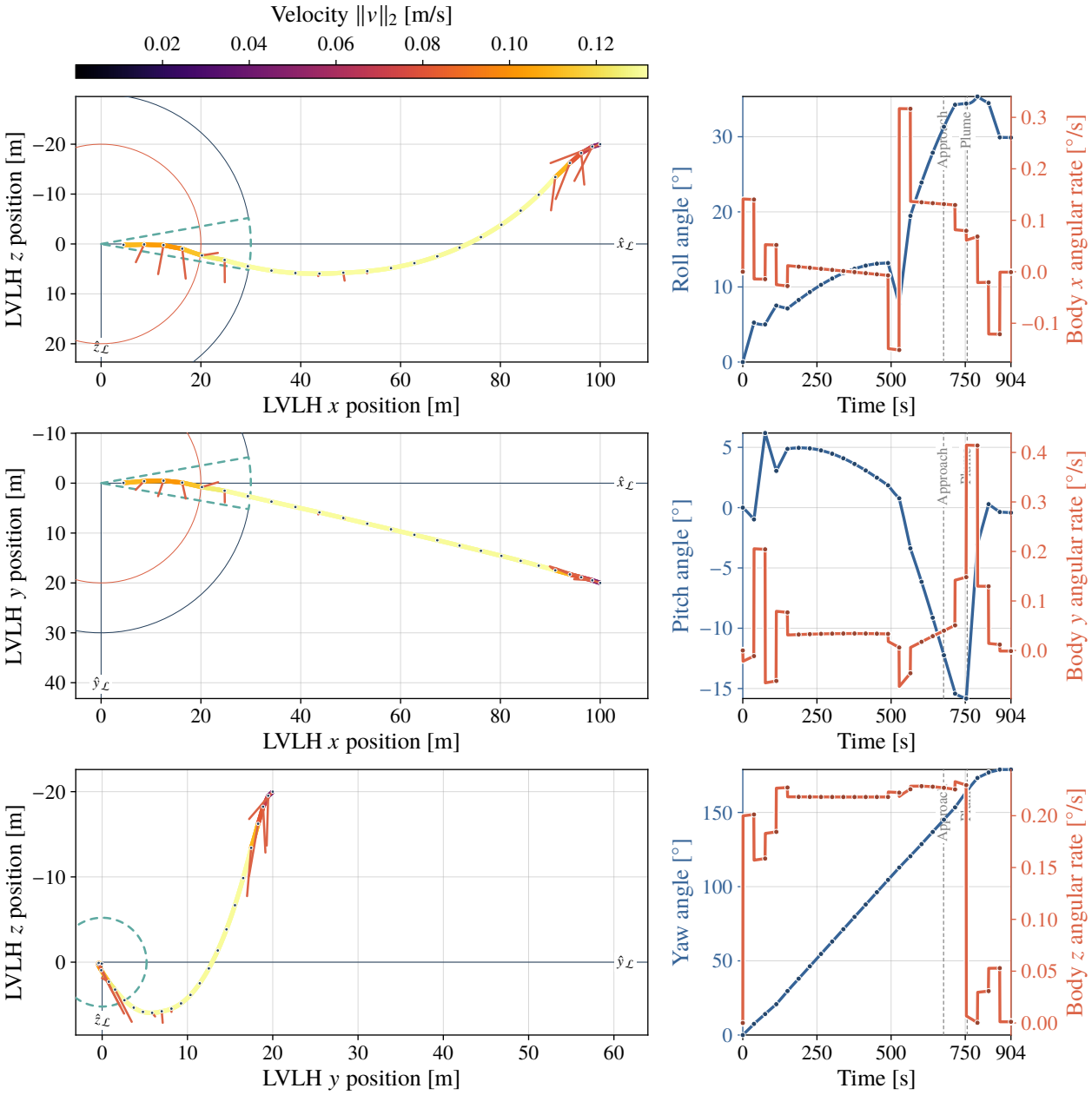


Fig. 15 Projected views of the optimized trajectory in the LVLH frame (left) and the corresponding evolution of the chaser's attitude (right).

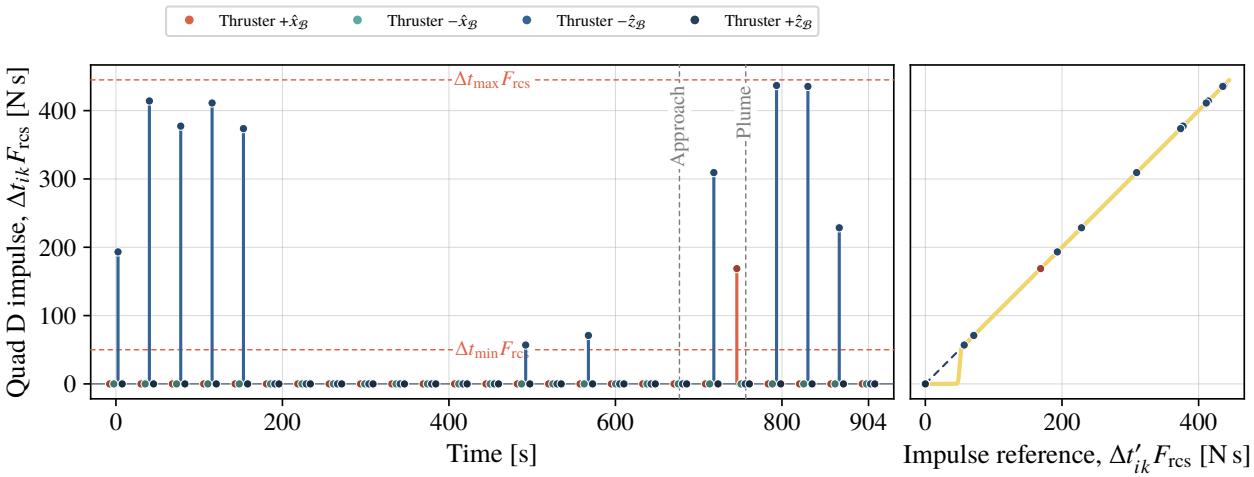


Fig. 16 RCS thruster firing history for quad D of Figure 14, shown in terms of the impulse $F_{\text{rcs}}\Delta t_{ik}$. In the left plot, the four thrusters are "spread" along the time axis in order to not overlap.

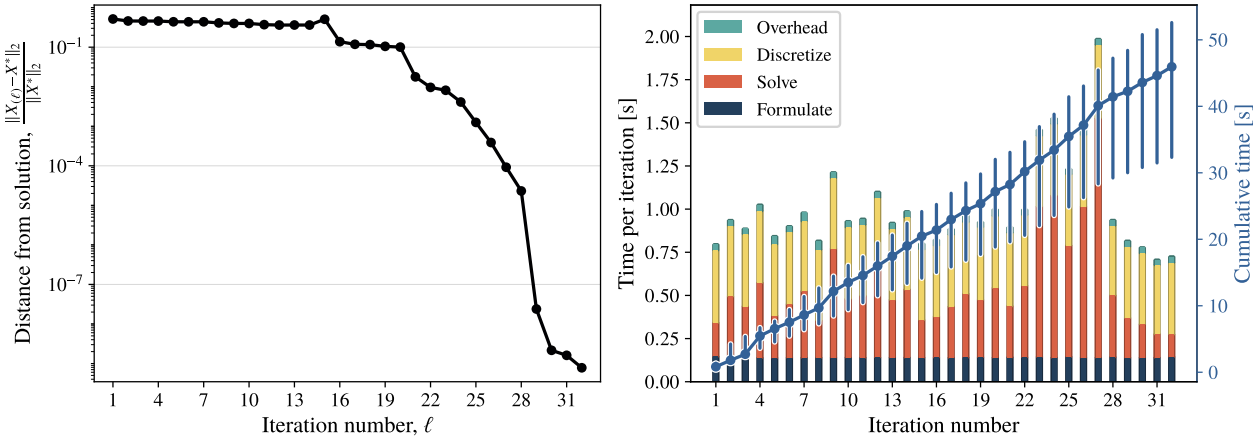


Fig. 17 Convergence and runtime performance of our algorithm. The runtimes show statistics over 20 executions. Median values are shown, and error bars show the 10% (bottom) and 90% (top) quantiles.

is the sum of the Solve bars in Figure 17). This corresponds to the time taken by the ECOS convex solver, which is written in C. We view this as a favorable runtime result for the following reasons, which we state based on experience from [52]. ECOS is a generic solver, and a custom solver is likely to run at least twice as fast [60, 61]. Coupled with other implementation efficiencies, we expect that the total solver time can be reduced to < 5 s. Furthermore, our code is optimized for readability. By writing other parts of the algorithm in a compiled language and optimizing for speed, we can expect to shrink the other 36 s of runtime down to < 5 s as well. Thus, a speed-optimized implementation of our algorithm can likely solve the rendezvous problem in under 10 s, which is quite acceptable for rendezvous applications since the actual trajectory can last for several thousand seconds.

Figure 18 shows the evolution of the cost function value over the PTR iterations. Every time the cost improvement falls within the decision range of (47), the homotopy parameter is updated. The update is followed by a spike in the cost, with fast subsequent improvement to an equal or better (i.e., smaller) value. During the final stages of the optimization

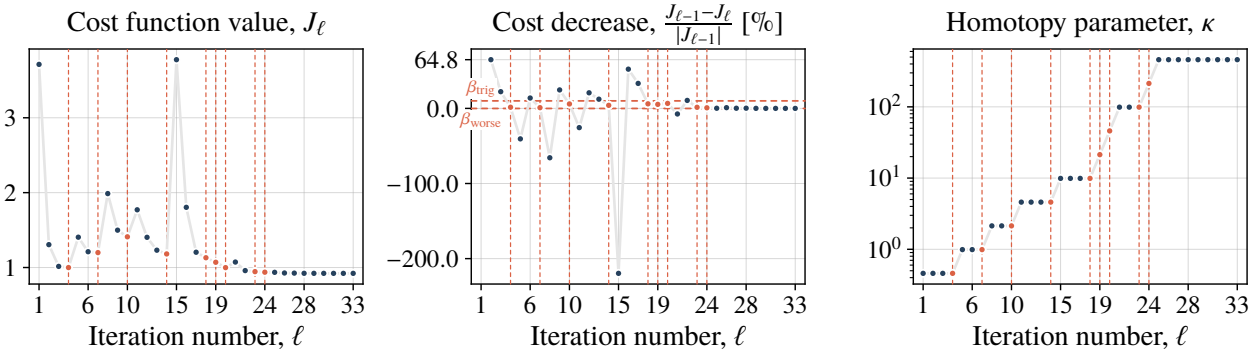


Fig. 18 Evaluation of the cost function (41a) over the PTR iterations (note the log scale for κ). Homotopy parameter updates are highlighted by red dashed vertical lines and markers.

(iterations $\ell \geq 18$), increases in κ no longer cause appreciable spikes in cost. This is remarkable, given that it is over these iterations that the homotopy parameter experiences its largest growth (since it grows exponentially, as seen in Figure 12b and the log scale of the rightmost plot in Figure 18). This means that, well before convergence occurs, our algorithm already finds a solution that is feasible with respect to the final "sharp" approximation of the discrete logic. This analysis is corroborated by the left plot in Figure 17, where it can be seen that past iteration $\ell \approx 20$ the amount by which the solution changes drops off quickly.

Finally, Figure 19 analyzes the depence of the optimal solution and of our algorithm's performance on the choice of homotopy update tolerance β_{trig} in (47). This reveals several favorable properties of the algorithm. First, by increasing β_{trig} we can dramatically lower the total iteration count and speed up the solution time. A very low value of β_{trig} emulates the non-embedded numerical continuation scheme from Figure 11a, since κ does not update until PTR has quasi-converged for its current value. By increasing β_{trig}, we can lower the iteration count by over 60% for this rendezvous example. We observe this behavior consistenly across different initial conditions. At the same time as lowering the iteration count, we basically maintain a consistent level of fuel-optimality. The fuel consumption goes up and down slightly, but on balance there is no perceptible trend. A notable downside of using a larger β_{trig} is an increased danger of not converging to a feasible trajectory, since we have "rushed" the algorithm too much. This does not happen in the present example, but we have noticed the issue for other initial conditions. Our future work plans to investigate what is the theoretically safe upper bound for the β_{trig} value.

VI. Conclusion

This paper presents a novel algorithm combining sequential convex programming with numerical continuation to handle a general class of discrete logic constraints in a continuous optimization framework. This makes the approach amenable to fast and reliable solution methods for trajectory optimization problems commonly encountered in spaceflight. The algorithm is applied to the terminal phase of rendezvous and docking maneuver, where a chaser spacecraft docks

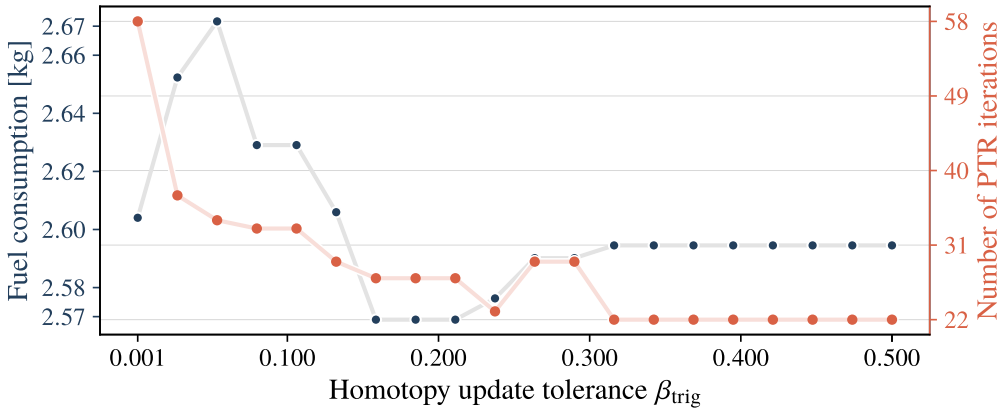


Fig. 19 Dependence of the converged trajectory's fuel consumption and of our algorithm's total iteration count on the value of β_{trig} in (47).

with a target subject to the following discrete logic constraints: thruster minimum impulse-bit, approach cone, and plume impingement. The algorithm is demonstrated for a realistic setup inspired by the Apollo Transposition and Docking maneuver. Fuel-optimal trajectories are generated with favorable runtimes that indicate a potential for real-time performance. The associated open-source implementation can be used as a ground-based analysis tool, and can be further optimized for onboard autonomous docking guidance.

Acknowledgments

The authors would like to extend their gratitude to Michael Szmuk and Taylor P. Reynolds for sharing their expertise in sequential convex programming and for their work on the initial conference paper [26].

References

[1] Woffinden, D. C., and Geller, D. K., "Navigating the road to autonomous orbital rendezvous," *Journal of Spacecraft and Rockets*, Vol. 44, No. 4, 2007, pp. 898–909. https://doi.org/10.2514/1.30734.

[2] Goodman, J. L., "History of space shuttle rendezvous and proximity operations," *Journal of Spacecraft and Rockets*, Vol. 43, No. 5, 2006, pp. 944–959. https://doi.org/10.2514/1.19653.

[3] D'Souza, C. N., Hanak, F. C., Spehar, P., Clark, F. D., and Jackson, M., "Orion rendezvous, proximity operations, and docking design and analysis," *AIAA Guidance, Navigation and Control Conference*, Hilton Head, SC, 2007, pp. 1–13. https://doi.org/10.2514/6.2007-6683.

[4] Weitering, H., "SpaceX's 1st upgraded Dragon cargo ship docks itself at space station with science, goodies and new airlock," https://www.space.com/spacex-cargo-dragon-crs-21-docks-at-space-station, Dec. 2020.

[5] Nishida, S.-I., and Kawamoto, S., "Strategy for capturing of a tumbling space debris," *Acta Astronautica*, Vol. 68, No. 1-2, 2011, pp. 113–120. https://doi.org/10.1016/j.actaastro.2010.06.045.

[6] Kaplan, M., "Survey of Space Debris Reduction Methods," *AIAA SPACE 2009 Conference & Exposition*, American Institute of Aeronautics and Astronautics, 2009, pp. 1–11. https://doi.org/10.2514/6.2009-6619.

[7] Chang, K., "An Orbital Rendezvous Demonstrates a Space Junk Solution," https://www.nytimes.com/2020/02/26/science/mev-1-northrop-grumman-space-junk.html, Feb. 2020.

[8] Malyuta, D., "SCP for Trajectory Optimization," https://github.com/dmalyuta/scp_traj_opt/tree/jgcd, 2021.

[9] Malyuta, D., Reynolds, T. P., Szmuk, M., Lew, T., Bonalli, R., Pavone, M., and Acikmese, B., "Convex Optimization for Trajectory Generation," *IEEE Control Systems Magazine (work in progress)*, 2021.

[10] Miele, A., Weeks, M. W., and Ciarcià, M., "Optimal trajectories for spacecraft rendezvous," *Journal of Optimization Theory and Applications*, Vol. 132, No. 3, 2007, pp. 353–376. https://doi.org/10.1007/s10957-007-9166-4.

[11] Miele, A., Ciarcià, M., and Weeks, M. W., "Guidance trajectories for spacecraft rendezvous," *Journal of Optimization Theory and Applications*, Vol. 132, No. 3, 2007, pp. 377–400. https://doi.org/10.1007/s10957-007-9165-5.

[12] Pascucci, C. A., Szmuk, M., and Açıkmeşe, B., "Optimal real-time force rendering for on-orbit structures assembly," *10th International ESA Conference on Guidance, Navigation & Control Systems*, ESA, 2017, pp. 1–9.

[13] Harris, M. W., and Açıkmeşe, B., "Minimum Time Rendezvous of Multiple Spacecraft Using Differential Drag," *Journal of Guidance, Control, and Dynamics*, Vol. 37, No. 2, 2014, pp. 365–373. https://doi.org/10.2514/1.61505.

[14] Lu, P., and Liu, X., "Autonomous Trajectory Planning for Rendezvous and Proximity Operations by Conic Optimization," *Journal of Guidance, Control, and Dynamics*, Vol. 36, No. 2, 2013, pp. 375–389. https://doi.org/10.2514/1.58436.

[15] Liu, X., and Lu, P., "Robust Trajectory Optimization for Highly Constrained Rendezvous and Proximity Operations," *AIAA Guidance, Navigation, and Control (GNC) Conference*, American Institute of Aeronautics and Astronautics, 2013, pp. 1–18. https://doi.org/10.2514/6.2013-4720.

[16] Breger, L. S., and How, J. P., "Safe trajectories for autonomous rendezvous of spacecraft," *Journal of Guidance, Control, and Dynamics*, Vol. 31, No. 5, 2008, pp. 1478–1489. https://doi.org/10.2514/1.29590.

[17] Richards, A., Schouwenaars, T., How, J. P., and Feron, E., "Spacecraft trajectory planning with avoidance constraints using mixed-integer linear programming," *Journal of Guidance, Control, and Dynamics*, Vol. 25, No. 4, 2002, pp. 755–764. https://doi.org/10.2514/2.4943.

[18] Sun, C., Dai, R., and Lu, P., "Multi-phase spacecraft mission optimization by quadratically constrained quadratic programming," *AIAA Scitech Forum*, San Diego, CA, 2019, pp. 1–15. https://doi.org/10.2514/6.2019-1667.

[19] Phillips, J., Kavraki, L., and Bedrossian, N., "Spacecraft Rendezvous and Docking with Real-Time, Randomized Optimization," *AIAA Guidance, Navigation, and Control Conference and Exhibit*, American Institute of Aeronautics and Astronautics, 2003, pp. 1–11. https://doi.org/10.2514/6.2003-5511.

[20] Hartley, E. N., Gallieri, M., and Maciejowski, J. M., "Terminal spacecraft rendezvous and capture with LASSO model predictive control," *International Journal of Control*, Vol. 86, No. 11, 2013, pp. 2104–2113. https://doi.org/10.1080/00207179.2013.789608.

[21] Bengea, S. C., and DeCarlo, R. A., "Optimal control of switching systems," *Automatica*, Vol. 41, No. 1, 2005, pp. 11–27. https://doi.org/10.1016/j.automatica.2004.08.003, URL https://doi.org/10.1016/j.automatica.2004.08.003.

[22] Saranathan, H., and Grant, M. J., "Relaxed Autonomously Switched Hybrid System Approach to Indirect Multiphase Aerospace Trajectory Optimization," *Journal of Spacecraft and Rockets*, Vol. 55, No. 3, 2018, pp. 611–621. https://doi.org/10.2514/1.a34012.

[23] Taheri, E., Junkins, J. L., Kolmanovsky, I., and Girard, A., "A novel approach for optimal trajectory design with multiple operation modes of propulsion system, part 1," *Acta Astronautica*, Vol. 172, 2020, pp. 151–165. https://doi.org/10.1016/j.actaastro.2020.02.042.

[24] Arya, V., Taheri, E., and Junkins, J. L., "A composite framework for co-optimization of spacecraft trajectory and propulsion system," *Acta Astronautica*, Vol. 178, 2021, pp. 773–782. https://doi.org/10.1016/j.actaastro.2020.10.007.

[25] Szmuk, M., Reynolds, T. P., and Açıkmeşe, B., "Successive Convexification for Real-Time Six-Degree-of-Freedom Powered Descent Guidance with State-Triggered Constraints," *Journal of Guidance, Control, and Dynamics*, Vol. 43, No. 8, 2020, pp. 1399–1413. https://doi.org/10.2514/1.g004549.

[26] Malyuta, D., Reynolds, T. P., Szmuk, M., Acikmese, B., and Mesbahi, M., "Fast Trajectory Optimization via Successive Convexification for Spacecraft Rendezvous with Integer Constraints," *AIAA Scitech 2020 Forum*, American Institute of Aeronautics and Astronautics, 2020, pp. 1–24. https://doi.org/10.2514/6.2020-0616.

[27] Szmuk, M., "Successive Convexification & High Performance Feedback Control for Agile Flight," Ph.D. thesis, University of Washington, Seattle, WA, 2019.

[28] Reynolds, T. P., Szmuk, M., Malyuta, D., Mesbahi, M., Açıkmeşe, B., and Carson, J. M., "Dual Quaternion-Based Powered Descent Guidance with State-Triggered Constraints," *Journal of Guidance, Control, and Dynamics*, Vol. 43, No. 9, 2020, pp. 1584–1599. https://doi.org/10.2514/1.g004536.

[29] Reynolds, T. P., "Computation Guidance and Control for Aerospace Systems," Ph.D. thesis, University of Washington, Seattle, WA, 2021.

[30] Szmuk, M., Reynolds, T. P., Acikmese, B., Mesbahi, M., and Carson, J. M., "Successive Convexification for 6-DoF Powered Descent Guidance with Compound State-Triggered Constraints," *AIAA Scitech 2019 Forum*, American Institute of Aeronautics and Astronautics, 2019, pp. 1–16. https://doi.org/10.2514/6.2019-0926.

[31] Szmuk, M., Malyuta, D., Reynolds, T. P., Mceowen, M. S., and Acikmese, B., "Real-Time Quad-Rotor Path Planning Using Convex Optimization and Compound State-Triggered Constraints," *2019 IEEE/RSJ International Conference on Intelligent Robots and Systems (IROS)*, IEEE, 2019, pp. 7666–7673. https://doi.org/10.1109/iros40897.2019.8967706.

[32] Betts, J. T., "Survey of numerical methods for trajectory optimization," *Journal of Guidance, Control, and Dynamics*, Vol. 21, No. 2, 1998, pp. 193–207. https://doi.org/10.2514/2.4231.

[33] Pontryagin, L. S., Boltyanskii, V. G., Gamkrelidze, R. V., and Mishchenko, E. F., *The Mathematical Theory of Optimal Processes*, Gordon and Breach Science Publishers, Montreux, 1986. https://doi.org/10.1201/9780203749319.

[34] Berkovitz, L. D., *Optimal Control Theory*, Springer New York, 1974. https://doi.org/10.1007/978-1-4757-6097-2.

[35] *CSM/LM Spacecraft Operation Data Book, Volume 3: Mass Properties*, National Aeronautics and Space Administration, SNA-8-D-027(III) REV 2 ed., 1969.

[36] Curtis, H. D., *Orbital Mechanics for Engineering Students*, 3rd ed., Butterworth-Heinemann, Waltham, MA, 2014.

[37] Solà, J., "Quaternion kinematics for the error-state Kalman filter," *CoRR*, 2017.

[38] *CSM/LM Spacecraft Operation Data Book, Volume 1: CSM Data Book, Part 1: Constraints and Performance*, National Aeronautics and Space Administration, SNA-8-D-027(I) REV 3 ed., 1970.

[39] *Apollo CSM and LM News Reference: Reaction Control Subsystem*, Space Division of North American Rockwell Corp., 1969.

[40] *Apollo Operations Handbook, Block II Spacecraft, Volume 1: Spacecraft Description*, National Aeronautics and Space Administration, SM2A-03-Block II-(1) ed., 1969.

[41] Boyd, S., and Vandenberghe, L., *Convex Optimization*, Cambridge University Press, Cambridge, UK, 2004.

[42] Nocedal, J., and Wright, S., *Numerical Optimization*, Springer New York, 1999. https://doi.org/10.1007/978-0-387-40065-5.

[43] Achterberg, T., and Wunderling, R., "Mixed Integer Programming: Analyzing 12 Years of Progress," *Facets of Combinatorial Optimization*, Springer Berlin Heidelberg, 2013, pp. 449–481. https://doi.org/10.1007/978-3-642-38189-8_18.

[44] Schouwenaars, T., Moor, B. D., Feron, E., and How, J., "Mixed integer programming for multi-vehicle path planning," *2001 European Control Conference (ECC)*, IEEE, 2001, pp. 2603–2608. https://doi.org/10.23919/ecc.2001.7076321.

[45] Schouwenaars, T., "Safe trajectory planning of autonomous vehicles," Dissertation (Ph.D.), Massachusetts Institute of Technology, 2006.

[46] Malyuta, D., and Açıkmeşe, B., "Approximate Multiparametric Mixed-Integer Convex Programming," *IEEE Control Systems Letters*, Vol. 4, No. 1, 2020, p. arXiv:1902.10994. https://doi.org/10.1109/lcsys.2019.2922639.

[47] Harris, M. W., "Optimal Control on Disconnected Sets using Extreme Point Relaxations and Normality Approximations," *IEEE Transactions on Automatic Control*, 2021, pp. 1–1. https://doi.org/10.1109/tac.2021.3059682.

[48] Malyuta, D., and Açikmeşe, B., "Lossless Convexification of Optimal Control Problems with Semi-continuous Inputs," *IFAC-PapersOnLine*, Vol. 53, No. 2, 2020, pp. 6843–6850. https://doi.org/10.1016/j.ifacol.2020.12.341.

[49] Blackmore, L., Açıkmeşe, B., and Carson III, J. M., "Lossless convexification of control constraints for a class of nonlinear optimal control problems," *Systems & Control Letters*, Vol. 61, No. 8, 2012, pp. 863–870. https://doi.org/10.1016/j.sysconle.2012.04.010.

[50] Harris, M. W., "Lossless Convexification of Optimal Control Problems," Ph.D. thesis, The University of Texas at Austin, Austin, 2014.

[51] Malyuta, D., Yu, Y., Elango, P., and Açıkmeşe, B., "Advances in Trajectory Optimization for Space Vehicle Control," *Annual Reviews in Control*, 2021. Accepted.

[52] Reynolds, T. P., Malyuta, D., Mesbahi, M., Açıkmeşe, B., and Carson III, J. M., "A Real-Time Algorithm for Non-Convex Powered Descent Guidance," *AIAA SciTech Forum*, AIAA, 2020, pp. 1–24. https://doi.org/10.2514/6.2020-0844.

[53] Hastie, T., Tibshirani, R., and Friedman, J., *The Elements of Statistical Learning*, 2nd ed., Springer New York, 2009. https://doi.org/10.1007/978-0-387-84858-7.

[54] Betts, J. T., *Practical Methods for Optimal Control Using Nonlinear Programming*, SIAM, 2020.

[55] Watson, L. T., "Numerical Linear Algebra Aspects of Globally Convergent Homotopy Methods," *SIAM Review*, Vol. 28, No. 4, 1986, pp. 529–545. https://doi.org/10.1137/1028157.

[56] Conn, A. R., Gould, N. I. M., and Toint, P. L., *Trust Region Methods*, SIAM, Philadelphia, PA, 2000. https://doi.org/10.1137/1.9780898719857.

[57] Kochenderfer, M. J., and Wheeler, T. A., *Algorithms for Optimization*, The MIT Press, Cambridge, Massachusetts, 2019.

[58] Bezanson, J., Edelman, A., Karpinski, S., and Shah, V. B., "Julia: A fresh approach to numerical computing," *SIAM review*, Vol. 59, No. 1, 2017, pp. 65–98. https://doi.org/10.1137/141000671.

[59] Domahidi, A., Chu, E., and Boyd, S., "ECOS: An SOCP solver for embedded systems," *2013 European Control Conference (ECC)*, IEEE, 2013, pp. 3071–3076. https://doi.org/10.23919/ecc.2013.6669541.

[60] Dueri, D., Zhang, J., and Açikmese, B., "Automated Custom Code Generation for Embedded, Real-time Second Order Cone Programming," *IFAC Proceedings Volumes*, Vol. 47, No. 3, 2014, pp. 1605–1612. https://doi.org/10.3182/20140824-6-za-1003.02736.

[61] Dueri, D., Açıkmeşe, B., Scharf, D. P., and Harris, M. W., "Customized Real-Time Interior-Point Methods for Onboard Powered-Descent Guidance," *Journal of Guidance, Control, and Dynamics*, Vol. 40, No. 2, 2017, pp. 197–212. https://doi.org/10.2514/1.g001480.